Impact of cloud presence on sky radiances and the retrieval of aerosol properties

Sara Herrero-Anta [a,b,*], Roberto Román [a,b], Daniel González-Fernández [a,b], Claudia Emde [c,d], David Mateos [a,b], Celia Herrero del Barrio [a,b], Ramiro González [a,b], Oleg Dubovik [e,f], Carlos Toledano [a,b], Abel Calle [a,b], Victoria E. Cachorro [a,b], Bernhard Mayer [c], Ángel M. de Frutos [a,b]

[a] *Grupo de O´ptica Atmosf´erica (GOA), Universidad de Valladolid, Valladolid 47011, Spain*
[b] *Laboratory of Disruptive Interdisciplinary Science (LaDIS), Universidad de Valladolid, Valladolid 47011, Spain*
[c] *Meteorological Institute, Ludwig-Maximilians-University, Munich D-80333, Germany*
[d] *German Aerospace Center (DLR-IPA), Oberpfaffenhofen D-82234, Germany*
[e] *GRASP-SAS, Lezennes 59260, France*
[f] *Laboratoire d'Optique Atmosph´erique (LOA), Universit´e de Lille, Lille 8518, France*

* Corresponding author at: Grupo de Óptica Atmosferica (GOA), Universidad de Valladolid, Valladolid 47011, Spain.
E-mail address: sara@goa.uva.es (S. Herrero-Anta).

Keywords: Sky radiance; Enhancement effect; Aerosols; Clouds; GRASP

A B S T R A C T

This paper explores the influence of the presence of clouds on sky radiances. It also analyses their impact on the retrieval of aerosol properties when using an inversion algorithm whose radiative transfer model (RTM) is designed for cloud-free atmospheres. For that, synthetic observations are simulated for 9 partially cloudy skies and for their equivalent cloud-free skies, considering 16 different aerosol scenarios. A parameter named cloud enhancement factor (CEF) has been used to determine the modifications induced in the sky radiances by each partially cloudy scenario with respect to the cloud-free sky. This parameter indicates that the sky radiances remaining after applying a cloud-screening are affected by the presence of clouds. In general, they show en-hancements between 0 and 20 % with respect to the cloud-free radiances, depending on the cloudy conditions and the scattering angle. The synthetic observations used as input for the retrieval of aerosol properties are the ones required by the inversion strategy used, GRASP$_{pac}$: the aerosol optical depth (AOD) and sky radiances at 4 different wavelengths together with the ceilometer range corrected signal (RCS). In partially cloudy scenarios with low CEFs, the aerosol properties do not present significant changes with respect to the cloud-free conditions. However, for partially cloudy scenarios with higher CEFs, a clear differentiation between the aerosol optical properties retrieved with and without clouds is observed. In these scenarios, the precision of the retrieval is similar for both conditions, but the accuracy is lower for the cloudy conditions. In particular, under partially cloudy conditions, it is observed an overestimation of the real refractive index (RRI) and the single scattering albedo (SSA) between 0.05 and 0.06 and between 0.03 and 0.06 respectively, and an underestimation of the asymmetry factor (g) and the imaginary refractive index (IRI) of about −0.02 and − 0.005, respectively. These values slightly vary with the aerosol load and wavelength for the RRI and SSA. The effects on the size distribution parameters are very small, concluding that the impact of clouds is noticeable in the optical properties but not so much in the microphysical part.

Abbreviations: GOA, Grupo de Óptica Atmosfe´rica; LaDis, Laboratory of Disruptive Interdisciplinary Science; DLR-IPA, German Aerospace Center; LOA, Laboratoire d'Optique Atmosph´erique; RTM, Radiative Transfer Models; CEF, Cloud Enhancement Factor; AOD, Aerosol Optical Depth; AOD_{440}, Aerosol Optical Depth at 440 nm; RCS, Range Corrected Signal; RRI, Real Refractive Index; IRI, Imaginary Refractive Index; SSA, Single Scattering Albedo; g, Asymmetry factor; IPCC, Intergovernmental Panel on Climate Change; AERONET, AErosol RObotic NETwork; GRASP, Generalized Retrieval of Atmosphere and Surface Properties; L, Sky radiances; I, Sun irradiance; MYSTIC, Monte Carlo code for the phYSically correct Tracing of photons In Cloudy atmospheres; libRadtran, library for Radiative transfer; VC, Volume Concentration; r, Volume median radius; Sigma, Standard deviation of log-normal distribution; VROOM, Variance Reduction Optimal Options Method; ZAMB, African Savanna, Zambia; SOLV, Solar Village, Saudi Arabia; GSFC, Goddard Space Flight Center, Maryland, USA; LANA, Lanai, Hawaii, USA; LWC, Liquid Water Content; COD, Cloud Optical Depth; Sph, Spherical particle fraction; CF, Cloud Fraction; CBH, Cloud Base Height; CTH, Cloud Top Height; R_{eff}, Effective radius; Lambda, Wavelength; SZA, Solar Zenith Angle; SAA, Solar Azimuth Angle.

1. Introduction

Atmospheric aerosols constitute the biggest source of uncertainty in the assessment of climate change as reported by the latest evaluation of the IPCC (Intergovernmental Panel on Climate Change; Forster et al., 2021). This large uncertainty is due to the high spatial and temporal variability of aerosols across the globe and the complexity of their in-teractions with solar radiation (aerosol–radiation interactions) and clouds (aerosol–cloud interactions) (Boucher et al., 2013). These in-teractions are related to the direct absorption and scattering of incoming solar radiation, as well as the modification of cloud properties, since they act as water droplet and ice crystal nuclei and therefore affect the cloud lifetime and albedo. The interactions depend on the aerosol load, and their optical and microphysical properties. These are variable as well with the aerosol type, and therefore a precise characterization and monitoring of aerosols on a global scale is of crucial importance.

Several techniques (in situ and remote sensing) and instruments (ground-based and onboard satellites) are used worldwide to monitor aerosols. Aerosol measurements from satellites are useful for achieving global coverage, but they usually present lower accuracy than ground-based observations. On the other hand, ground-based instruments are limited to a single-location, but they offer a high accuracy and precision, making them useful for having long-term data series, and to validate and/or calibrate data from satellites. All this motivated the creation of ground-based networks around the world to monitor aerosols.

One extended technique to derive aerosol properties is the use of photometers, which measure solar irradiance or even sky radiances at different wavelengths with narrow spectral filters. This passive remote sensing technique is used by one of the most extended monitoring net-works: AERONET (AErosol RObotic NETwork; Holben et al., 1998; Giles et al., 2019). The reference instrument of AERONET is the CE318 (*Cimel Electronique* manufacturer) ground-based sun-sky photometer. It is designed to measure, at several wavelengths, direct solar irradiance (I), but also lunar irradiance in the recent CE318-T models (Barreto et al., 2016; Roma´n et al., 2020; Gonza´lez et al., 2020), and diffuse sky radi-ances (L) at different sky points. The solar and lunar irradiances can be used to derive the aerosol optical depth (AOD) at different wavelengths during daytime and night-time, respectively, by applying the Beer-Bouguer-Lambert equation.

Diffuse sky radiance is mainly caused by the scattering of sunlight by gases, clouds and aerosols, hence sky radiances measurements contain valuable information about the aerosol properties. These measurements can be used in combination with AOD to retrieve advanced aerosol properties like single scattering albedo (SSA), complex refractive index (real part, RRI and imaginary part, IRI), asymmetry factor (g), or volume size distribution using inversion algorithms (Dubovik and King, 2000; Dubovik et al., 2002, 2006, 2021; Sinyuk et al., 2020). Most of these inversion algorithms are iterative methods that look for the set of aerosol properties that best reproduces the measurements given as input (in the case of AERONET, AOD and sky radiances). This method consists of a statistically optimized search of the set of properties that minimizes the residuals between the real measurements given as input and the mea-surements that would be reproduced for that set of properties. To this end, they use a radiative transfer model (RTM) to simulate the sky ra-diances and AOD for any set of aerosol properties. In general, the RTM used by inversion algorithms (like the used by AERONET) do not consider the presence of clouds, henceforth they conduct the radiative transfer simulations considering a cloud-free sky.

Despite input measurements are usually filtered out using cloud-screening criteria to remove those points where clouds are located, the presence of clouds can also modify the sky radiances at cloud-free points away from the clouds (Roman et al., 2022a). Since these modifications are not accounted for in the RTM, the inversion of these modified ra-diances would yield to a set of aerosol properties that might be different than the real ones. That is, the aerosol properties given by the inversion algorithm correspond to an aerosol scenario that would produce these modified sky radiances in a cloud-free sky. A precise knowledge of some aerosol properties is essential to accurately assess their radiative impact; therefore, utilizing aerosol properties retrieved under partially cloudy scenarios might introduce biases with respect to their real effect.

Some RTMs, like the 3D solver MYSTIC from libRadtran (Emde et al., 2016), allow the definition of clouds in order to conduct 3D radiative transfer simulations for cloudy conditions, which can be useful to determine the modifications induced by the presence of clouds in the sky radiances with respect to the cloud-free situation. This was previously considered by Grob et al. (2019) to investigate the impact of clouds on the retrieval of aerosol using polarimetric measurements. This frame-work motivates the main objective of this work, which is to analyse and quantify the effect of the presence of clouds in the sky radiances for partially cloudy skies and how the use of these sky radiances as input for inversion algorithms affects the retrieval of aerosol properties.

This work is organized as follows: the two algorithms to be utilized and the aerosol scenarios considered in the study are described in Section 2. Section 3 comprises the main results regarding the evaluation and characterization of the partially cloudy and cloud-free scenarios used for the retrieval of aerosol properties, and the evaluation of the properties obtained. Finally, the main conclusions of the work are summarized in Section 4.

2. Methodology

This section first describes the two algorithms used throughout the paper: GRASP (Section 2.1), where it is detailed the inversion strategy followed, and MYSTIC (Section 2.2). Afterwards, in Section 2.3, it is given an overview of the aerosol and cloudy scenarios used for the analysis. Finally, it is detailed the procedure used to simulate the observations that will be latter used as input for the inversion algorithm, following the described inversion strategy.

2.1. GRASP

GRASP (Generalized Retrieval of Atmosphere and Surface Proper-ties; Dubovik et al., 2014, 2021) is a versatile and flexible inversion algorithm designed to retrieve microphysical and optical aerosol prop-erties and optical surface properties. It mainly consists of two inde-pendent modules: the forward model, that carries out the radiative transfer simulations, and the numerical inversion module, which is used in combination with the forward module for the retrieval of aerosol properties.

The forward module is based on the "successive orders of scattering" approach (Lenoble et al., 2007; Herreras-Giralda et al., 2022), and ac-counts for multiple-scattering and light polarization. This forward module can be very useful to simulate synthetic measurements by providing the model with parameters that describe the atmospheric conditions: aerosols, gases and solar zenith angle (SZA) mainly. GRASP works with normalized radiances, thus, a factor must be applied to transform the output into radiance units and vice-versa if they are used as input for the inversion module (see Herrero-Anta et al., 2023).

The numerical inversion module is an iterative algorithm that uses the multi-term least squares method (Dubovik and King, 2000), based on the maximum likelihood method, to find a statistically optimized solution (the set of aerosol properties); i.e. the one that minimizes the re-sidual between the observations given as input and the synthetic observations reproduced by the forward module for that set of proper-ties. The optimization is achieved applying a Levenberg-Marquardt linear fitting on each iteration to optimize an initial guess vector (the initial set of aerosol properties). This method allows the use of constraints to restrict the range of possible values that some properties can take and as well as the smoothness in the variation of the properties with some parameter such as wavelength or radius. In the output GRASP returns the residual (see Roman et al., 2022b), which is a measure of the goodness of the fitting, and can be used to reject the inversions with a low convergence (high residual).

2.1.1. Inversion strategy

The inversion strategy used in this work is the so called $GRASP_{pac}$. It was developed and validated by Roman et al. (2018) to retrieve columnar and vertically resolved aerosol properties from the combina-tion of photometer and ceilometer measurements, hence its name pac. $GRASP_{pac}$ has already been used in different aerosol studies (Titos et al., 2019; Herreras et al., 2019; Bazo et al., 2023; Salgueiro et al., 2023) and even implemented in automatic processing systems to process data in near-real time (Herrero del Barrio et al., 2025).

The inputs for this inversion strategy are: the AOD and the sky ra-diances at 440, 675, 870 and 1020 nm measured from photometers, and the range corrected signal (RCS) at 1064 nm from a ceilometer. The sky radiances can be measured by photometers at different geometries. Here, only the sky radiances from the almucantar geometry (sky points with zenith angle equal to the solar zenith angle) at the scattering angles used by AERONET (Sinyuk et al., 2020) have been considered; i.e., those with azimuth angle (relative to the Sun) equal to: 3.5°, 4°, 5°, 6°, 7°, 8°, 10°, 12°, 14°, 16°, 18°, 20°, 25°, 30°, 35°, 40°, 45°, 50°, 60°, 70°, 80°, 90°, 100°, 120°, 140°, 160°. The sky radiances in the almucantar are measured in two symmetric branches with respect to the Sun, so that the value used for the inversion at each scattering angle is the mean of the pair of symmetric points. This symmetry is also used for AERONET cloud-screening criterion (Holben et al., 2006, level 1.5 of AERONET version 2), so that if the relative difference between a pair of symmetric points is higher than 20 %, the sky radiance corresponding to that scattering angle is rejected. The RCS is given at 60 log-spaced bins at different heights, as in Lopatin et al. (2013), between 250 m and 7000 m a.g.l., and normalized by the integrated RCS. A detailed description of the methodology can be accessed in Roma´n et al. (2018).

In order to evaluate whether the scenarios are suitable for inversion, AERONET applies a quality assurance criterion to the sky radiances remaining after cloud-screening. For each wavelength, it only considers the sky radiance distribution representative if there is at least one measurement in each of the following scattering angle regions: $\geq 3.2^{\circ}$ to 6°; $\geq 6^{\circ}$ to 30°; $\geq 30^{\circ}$ to 80°; and $\geq 80^{\circ}$. In this work the 80° scattering angle limits have been replaced by 78° to include scenarios with SZA = 40°, since for that solar elevation the 80 scattering angle corresponds to the 180° azimuth angle, which is not considered in the inversion (Rom´an et al., 2018). If the sky radiances for certain inversion do not satisfy the quality assurance criterion for the four wavelengths the inversion will be rejected.

$GRASP_{pac}$ gives as output a set of column-integrated properties and vertical profiles of extensive properties. We will focus here in the anal-ysis of the most representative: single scattering albedo, asymmetry factor, and complex refractive index at 440, 675, 870, 1020 and 1064 nm; and the volume size distribution which is assumed as a 22 triangle radius bins distribution. For the volume size distribution the bi-lognormal size distribution parameters have been extracted: volume median radius (r), standard deviation of log-normal distribution (σ) and aerosol volume concentration (VC), all for fine (f) and coarse (c) modes. The residual of the final inversion will be used as a quality assurance criterion for convergence; retrievals with a value higher than 10 % will be rejected.

2.2. libRadtran/MYSTIC

libRadtran (library for Radiative transfer; Mayer and Kylling, 2005; Emde et al., 2016) is a widely used software package for radiative transfer calculations. This package includes the radiative transfer solver MYSTIC (Monte Carlo code for the phYSically correct Tracing of photons In Cloudy atmospheres; Mayer, 2009; Emde et al., 2010), which allows 3D radiative transfer simulations by Monte Carlo techniques. It is ideal to estimate sky radiances under partially cloudy scenarios.

In this work we have used MYSTIC (libRadtran version 2.0.5) to simulate the same sky radiances used in the GRASP$_{pac}$ (see Section 2.1.1) under different aerosol conditions. These simulations have been done for different partially cloudy scenarios but also for their equivalent sce-narios without clouds. MYSTIC has been run with the Variance Reduc-tion Optimal Options Method (VROOM; Buras et al., 2011) using a total of one million of photons to be traced and a minimum value of photons to be used per sky radiance simulation. Polarization has been considered in the simulations (Emde et al., 2010).

2.3. Scenario description

In order to have a representative set of aerosol conditions, different aerosol types and loads have been considered for the inversion. Four aerosol types have been selected to cover a representative range of ab-sorption and size distribution properties, corresponding to the key aerosol types observed worldwide: urban, biomass burning, dust and oceanic. One kind from each of the mentioned aerosol types has been extracted from the climatology developed by Dubovik et al. (2002): African Savanna (ZAMB; Zambia) for biomass burning, Solar Village (SOLV; Saudi Arabia) for dust, Goddard Space Flight Center (GSFC; Maryland, USA) for urban, and Lanai (LANA; Hawaii, USA) for oceanic. These aerosol types are mainly characterized by their complex refractive index, the bimodal size distribution and the spherical particle fraction (fraction of sphere/non-sphere particles; Sph), all extracted from Torres et al. (2017).

Four scenarios with different aerosol loads have been created for each aerosol type, resulting in a total of 16 (4 $\times$ 4) aerosol scenarios. These aerosol loads correspond to AOD at 440 nm (AOD_{440}) values of 0.1
(low load), 0.2 (moderate load), 0.4 (high load) and 1.0 (extreme load). For simplicity, the aerosol has been assumed to be vertically distributed in a triangular layer with maximum concentration at 2 km a.g.l. and zero
at 1 km and 3 km a.g.l. In this study we have used the coordinates of Valladolid, Spain (41.6639° N, 4.7056° W), with an altitude of 0 m a.s.l. for the location. The surface reflectance has been assumed to be zero,
since we will use synthetic observations and for ground-based atmo-spheric measurements the reflected light is of second-order importance (Dubovik and King, 2000).

The inversion of aerosol properties is not usually carried out under high cloud cover conditions since a high amount of sky points are covered by a cloud or the sun is obstructed by clouds. Therefore, this study will be conducted only for partially cloudy skies with not obstructed Sun that overcome the cloud-screening and quality assurance criteria detailed in Section 2.1.1. 3D fields of partially cloudy skies have been extracted from the dataset by Jakub and Gregor (2022), which comprises a 6-h evolution of clouds with an ever increasing cloud deck, at times 90 (Cloud cover A), 150 (Cloud cover B) and 152 min (Cloud
cover C), represented in Fig. 1. These cloud fields are defined on a 256 $\times$
256 horizontal grid with a 25 m pixel resolution. The vertical resolution consists of 119 layers, ranging from 0 to 5.5 km a.g.l., with a resolution that varies from 25 m in the lowest layers to 78 m in the highest. The three cloudy scenarios correspond to shallow cumulus located about 1 km a.g.l. with low to moderate cloud presence (cloud fractions of 13.2
%, 36.5 % and 34.0 %, respectively) and different liquid water content (LWC) and cloud optical depths (COD) values (see Fig. 1). COD presents values about 10 in the Cloud cover A, while it reaches maximum values close to 50 and 40 in the B and C cases, respectively. More information about the cloud properties of the three Cloud cover cases is detailed in Table 1.

For each cloud cover, different Sun positions have been considered. Since the sky radiances in the points of the almucantar depend on the relative position of the Sun, this will determine different partially cloudy scenarios for the same cloud cover. Three different SZAs and solar azi-
muth angles (SAA) have been considered for each of the three cloud covers, resulting in a total of 9 (3 $\times$ 3) partially cloudy scenarios. The all-sky images simulated for these cloud covers can be seen in Fig. 2.

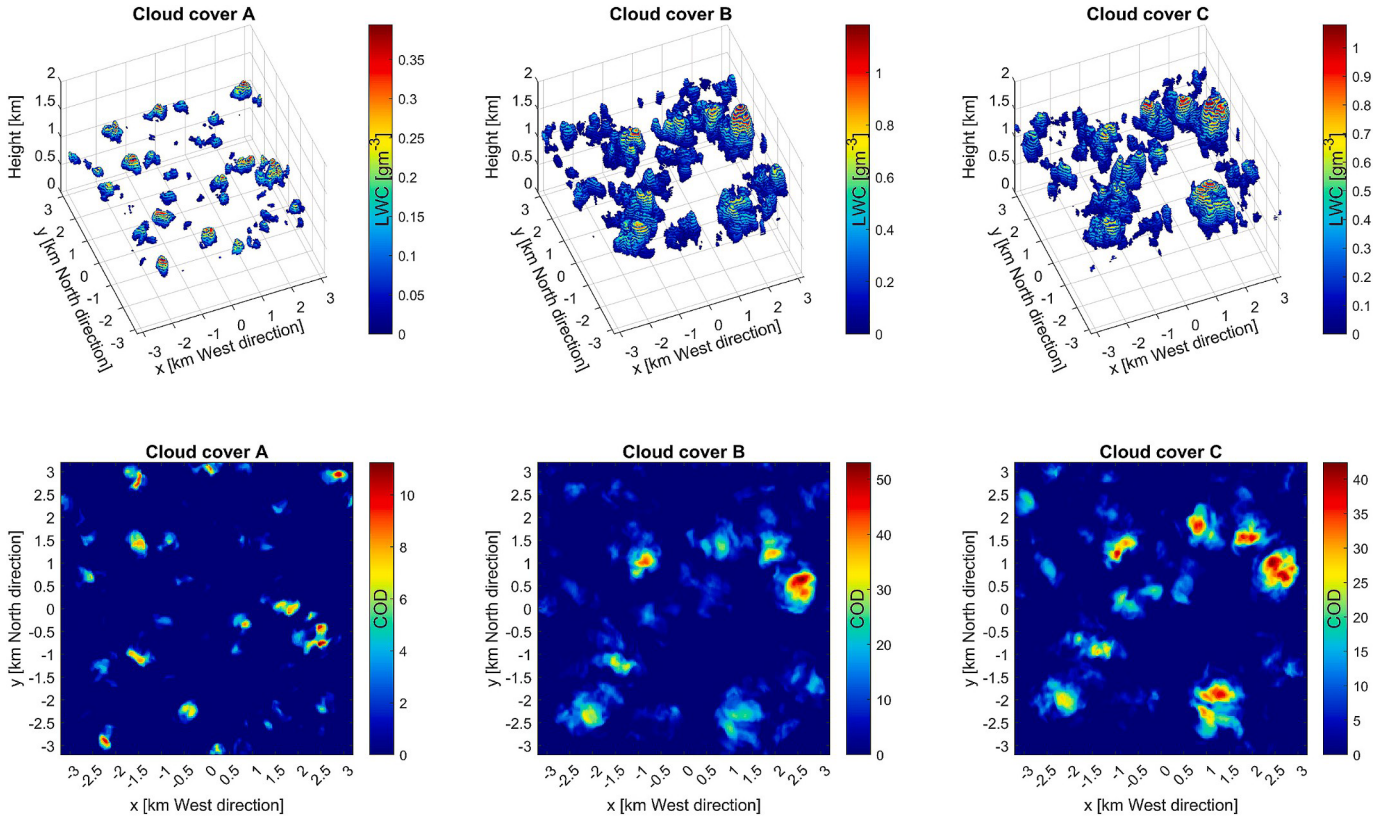

Fig. 1. Cloud liquid water content (LWC; upper panels) and vertically integrated cloud optical depth (COD; bottom panels) for the three cloudy scenarios: Cloud cover A (left), B (middle) and C (right).

Table 1

Overview of the aerosol and cloud cover properties used to create the analysed scenarios. The aerosol types include ZAMB (biomass burning), SOLV (dust), GSFC (urban), and LANA (oceanic), and are described by the real refractive index (RRI), imaginary refractive index (IRI), the bi-lognormal parameters of the volume size distribution (volume median radius (r), standard deviation of log-normal distribution (σ) and aerosol volume concentration (VC)) for the fine (f) and coarse (c) and the spherical particle fraction (Sph). The main characteristics of the cloud covers are: the relative Sun position, defined by the solar zenith angle (SZA) and the solar azimuth angle (SAA), the cloud fraction (CF), the cloud base (CBH) and top (CTH) heights, the maximum (and mean, in parenthesis) cloud optical depth (COD), the maximum (and mean, in parenthesis) liquid water content (LWC) and maximum (and mean, in parenthesis) effective radius (R_{eff}).

	AOD (440 nm)		RRI (440–1064 nm)	IRI (440–1064 nm)	r_f [μm]	r_c [μm]	σ_f [μm]	σ_c [μm]	VC_f [$\mu m^3/\mu m^2$]	VC_c [$\mu m^3/\mu m^2$]	Sph (%)
ZAMB	0.1, 0.2, 0.4, 1.0		1.51	0.0210	0.12 + 0.025 AOD_{440}	3.22 + 0.71 AOD_{440}	0.40	0.73	0.12 AOD_{440}	0.09 AOD_{440}	100
SOLV			1.56	0.0029	0.12	2.32	0.40	0.60	0.02 + 0.02 AOD_{440}	−0.02 + 0.98 AOD_{440}	0
GSFC			1.41–0.03 AOD_{440}	0.0030	0.12 + 0.11 AOD_{440}	3.03 + 0.49 AOD_{440}	0.38	0.75	0.15 AOD_{440}	0.01 + 0.04 AOD_{440}	100
LANA			1.36	0.0015	0.16	2.70	0.48	0.68	0.40 AOD_{440}	0.80 AOD_{440}	100
	SZA	**SAA**	**CF (%)**	**CBH** (*km a.g.l.*)	**CTH** (*km a.g.l.*)	**COD**	**LWC** (g/m^3)	**R_{eff}** (μm^3)			
	0	0									
	40	135									
Cloud cover A	55	135	13.2	0.846	1.188	11.243 (2.254)	0.394 (0.098)	10.150 (5.836)			
	70	135									
	40	45									
Cloud cover B	50	50	13.2	0.945	1.687	53.019 (7.450)	1.183 (0.227)	14.640 (7.674)			
	55	45									
	40	45									
Cloud cover C	50	50	34.0	0.945	1.606	42.417 (8.088)	1.080 (0.233)	14.200 (7.747)			
	55	90									

The 16 aerosol scenarios have been considered under the 9 partially cloudy scenarios, obtaining a total of 9 × 16 clouds-aerosol scenarios. A summary of the aerosol and cloud cover properties used to create the
scenarios has been included in Table 1.

2.4. Observations simulation

The inversion strategy used in this study, GRASP$_{pac}$, uses as input three different observations: sky radiances, AOD and RCS. These observations have been simulated using the two RTMs described in 2.1 and
2.2: GRASP and MYSTIC. The measurements have been generated for the 9 × 16 clouds-aerosol scenarios described in the previous section, but also for the equivalent cloud-free conditions, which will be used as
the reference retrieval. The RTM from GRASP has been used to simulate the sky radiances, AOD and RCS under cloud-free conditions. This module does not consider the clouds, therefore, MYSTIC has been used to simulate the sky radiances for cloudy conditions. The sky radiances
have been simulated with MYSTIC for the 9 × 16 clouds-aerosol scenarios and for the equivalent cloud-free situation, in order to calculate the enhancement induced by the presence of clouds. This enhancement will be added to the sky radiances simulated with GRASP in cloud-free conditions, to derive the synthetic observations under partially cloudy conditions. In this way, only the sky radiances are affected by clouds presence; the AOD and RCS are assumed to be unaffected.

The aerosol properties for the input to the forward module (RTM) from GRASP have been directly extracted from the climatology values of Dubovik et al. (2002), i.e.: the bimodal size distribution parameters for fine and coarse modes, the complex refractive index at 440, 675, 870, 1020 and 1064 nm, and the spherical particle fraction for the corre-sponding aerosol load and type. The aerosol properties at 1064 nm have been assumed to be equal as for 1020 nm, since they are not included in the climatology. The spherical particle fraction has been considered 0 for SOLV for all aerosol loads, as a simplification based on the values given in Torres et al. (2017). Finally, for the vertical aerosol distribution, the corresponding concentration at each altitude has been calculated for the assumed vertical triangular distribution and introduced by the RCS at 1064 nm as described in 2.1.

In MYSTIC, the aerosol properties are introduced by the AOD, the aerosol phase function and the single scattering albedo, all at 440, 675, 870 and 1020 nm. These parameters have been extracted from the output file given by the forward module from GRASP. Finally, the ver-tical aerosol distribution has been introduced by the fraction of aerosol concentration at each height.

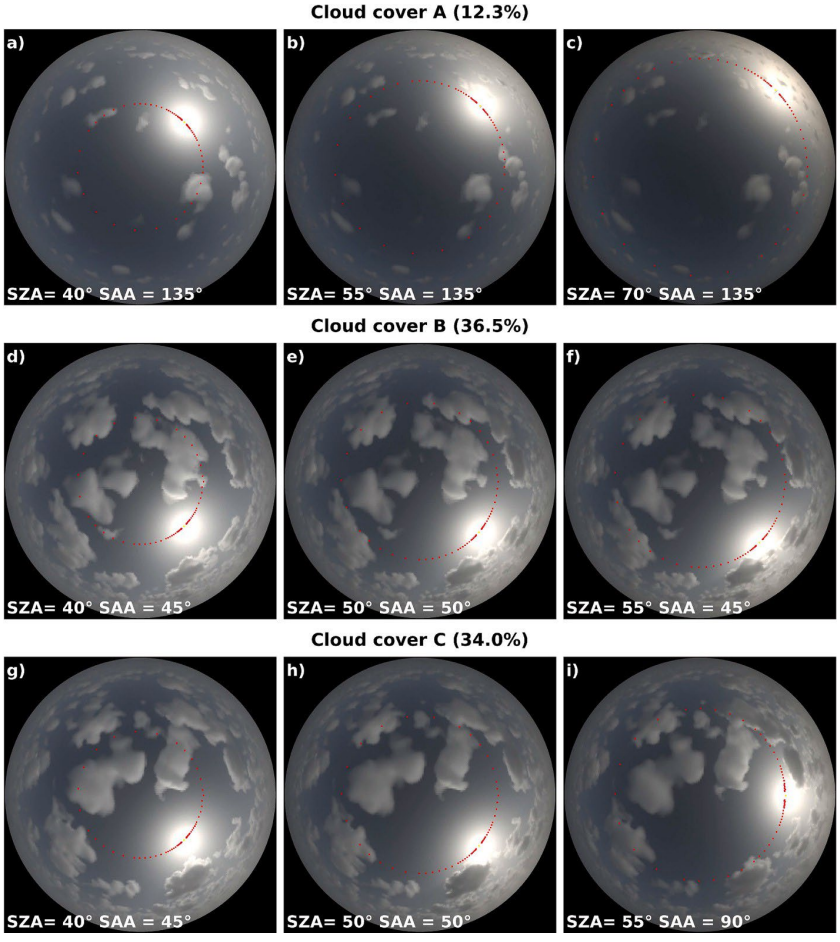

Fig. 2. Simulated all-sky images produced with MYSTIC for the 9 partially cloudy scenarios created with the 3 different cloud covers using different Sun positions (different solar zenith angle, SZA and solar azimuth angle, SAA), where the south direction corresponds to a SAA value of 0°: a)-c) Cloud cover A, d)-f) Cloud cover B, g)-i) Cloud cover C. The red points correspond to the sky points measured by CE318-T photometers in the almucantar geometry. The values in parenthesis indicate the cloud fraction of each cloud cover. (For interpretation of the references to colour in this figure legend, the reader is referred to the web version of this article.)

In this study, the input data used for the inversion correspond to synthetic measurements. Since real measurements have some uncer-tainty associated to the instrument, the synthetic observations have been perturbed. As we have used $GRASP_{pac}$ for the inversion, which was developed to use data from photometers and ceilometers, the uncertainty associated with these instruments has been used to introduce a Gaussian distributed random noise as described in Roman et al. (2018). A total of 200 perturbed sets of synthetic observations have been created for each of the original 9 $\times$ 16 sets of observations (without perturba-tion), assuming the instrumental uncertainty of the measurements as the perturbing noise (see Roman et al., 2018; Roman et al., 2022b; Herrero-Anta et al., 2023). The perturbed sky radiances from all cloud-free and partially cloudy synthetic observations have been subjected to the cloud-screening and quality assurance criteria in order to reject the observa-tions not suitable for the inversion.

3. Results

3.1. Cloud-free scenarios: Sky radiances comparison

As mentioned before, the RTM from GRASP does not consider the presence of clouds, and therefore it is necessary to use a 3D RTM like MYSTIC to simulate the sky radiances under partially cloudy skies. In order to check whether the two models are comparable, the sky radi-ances simulated with both models in the almucantar geometry for cloud-free conditions have been compared for the 16 aerosol scenarios and different SZA values (40°, 50°, 55° and 70°), in accordance with those used for the partially cloudy scenarios. The "2000 ASTM Standard Extraterrestrial Spectrum Reference E-490-00" (http://rredc.nrel.go v/solar/spectra/am0), has been used to convert the output from both RTMs into radiance physical units.

In Fig. 3 sky radiances from MYSTIC and GRASP have been plotted against the scattering angle at the photometer wavelengths for the ZAMB aerosol type with an AOD_{440} of 0.4 and a SZA value of 40°. Both sky radiances show a very similar behaviour at the four wavelengths, with slightly higher differences observed at the smallest scattering an-gles. For a detailed analysis the relative differences between MYSTIC and GRASP sky radiances ($\Delta L_{MYSTIC-GRASP}$) have been calculated and included in the panel b of Fig. 3. These differences are usually within $\pm$ 1% except for the two highest scattering angles, where they reach values of 2% and specially for those in the solar aureole region, that present values of almost 4%. These results are similar for all the wavelengths and they do not present a clear pattern. The observed differences might be partially caused by the random nature of the Monte Carlo method employed by MYSTIC, which also explains why the relative differences are not symmetric with the scattering angle.

For a global analysis of the correlation between both models, the average of the differences has been calculated considering the 16 available aerosol scenarios for each SZA. The mean values and the corresponding standard deviations obtained at each scattering angle and wavelength are shown in Fig. 4 for each SZA. The general behaviour is similar to the one obtained for the single aerosol scenario of Fig. 3, showing higher relative differences at the lowest and the highest scat-tering angles (> 70°), but generally within $\pm$2% for all the SZAs. Here it can be appreciated a dependence with respect to the SZA, showing lower differences for higher SZAs (lower Sun elevation), specially for the scattering angles in the solar aureole region.

3.2. Cloud enhancement factor under partially cloudy scenarios

The effect of the presence of clouds in the sky radiances has been quantified with a new parameter named cloud enhancement factor (CEF). It has been defined, for each wavelength and scattering angle, as the ratio of the sky radiance under cloudy conditions to the sky radiance under the equivalent scenario in cloud-free conditions. In this work, the CEFs in the almucantar geometry have been calculated using the sky radiances simulated with MYSTIC for the cloudy and cloud-free condi-tions for each of the 9 $\times$ 16 clouds-aerosol scenarios.

The sky radiances simulated in the almucantar for cloud-free and partially cloudy conditions (Cloud cover C with SZA = 50° and SAA = 50° for ZAMB aerosol type; Fig. 2h) are shown in Fig. 5 with their cor-responding CEF values for different AOD values. The sky radiances, shown in the upper panel, present sharp changes with the scattering angle for the partially cloudy conditions, which are related to the presence of clouds in those points of the sky (as can be seen in Fig. 2h). The sky radiances at these points are much higher than in the cloud-free conditions, where there is a smooth variation with respect to the scattering angle and, therefore, the corresponding CEFs are very high too. In the points where no clouds are located the differences in the sky radiances are not visually noticeable.

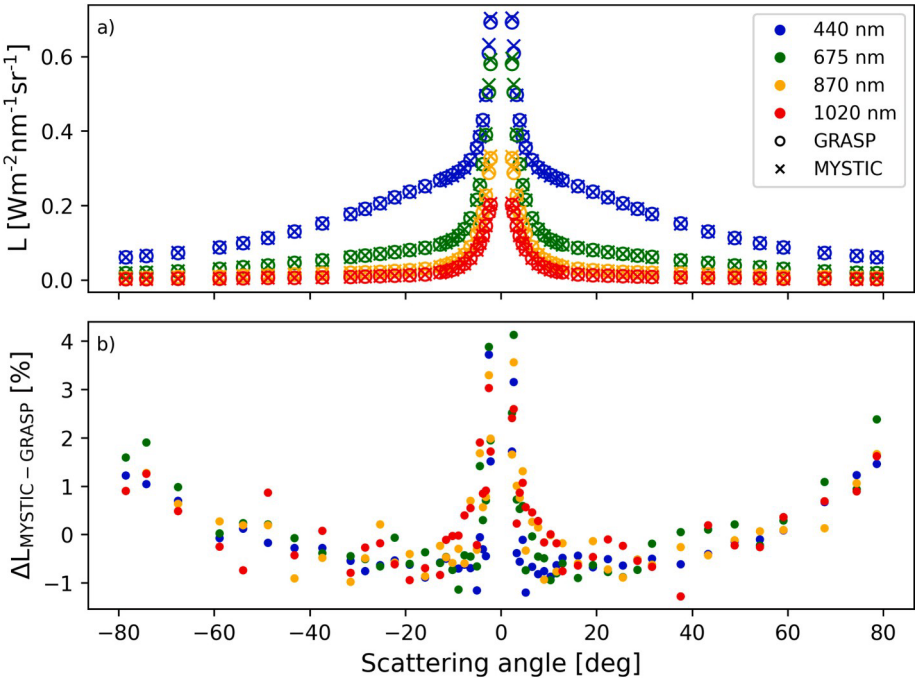

Fig. 3. a) Sky radiances (L) in the almucantar geometry simulated with MYSTIC (cross marker) and GRASP (circle marker) as a function of the scattering angle (negative angles represent negative azimuth values), at 440, 675, 870 and 1020 nm. The aerosol scenario corresponds to ZAMB under cloud-free conditions with an AOD at 440 nm of 0.4 and a solar zenith angle of 40° and b) the corresponding relative differences ($\Delta L_{MYSTIC-GRASP}$) between the MYSTIC and GRASP simulated sky radiances of the upper panel.

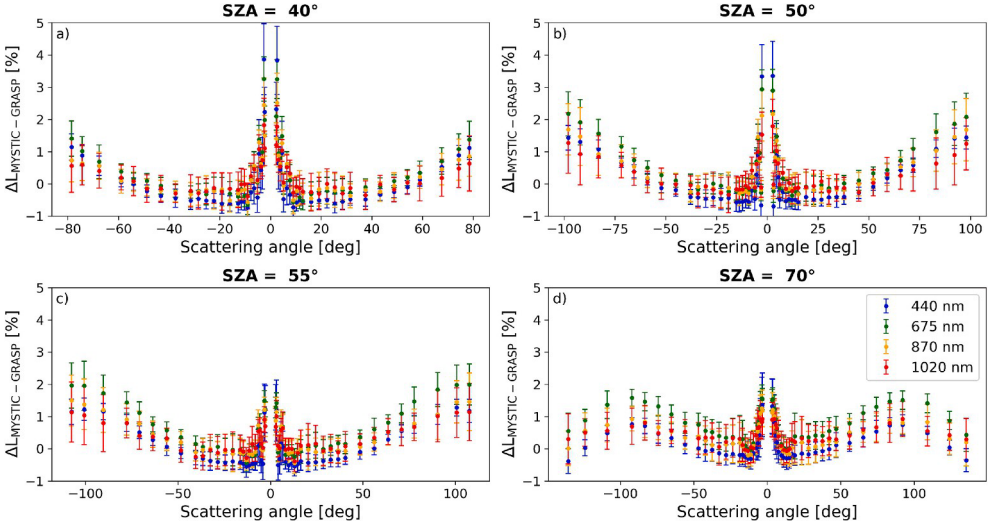

Fig. 4. Error bar plots of the mean relative differences between the sky radiances (L) simulated with MYSTIC and GRASP calculated considering the 16 different aerosol scenarios for solar zenith angle (SZA) equal to 40° (a), 50° (b), 55° (c) and 70° (d). The error bars represent the standard deviation of the average.

Fig. 5 also shows a decrease in CEF values when AOD increases. This is because more light is scattered by aerosols as the AOD increases, which increases the sky radiance in cloud-free conditions. Therefore, the ratio between the radiance in a point affected by clouds and the corre-sponding radiance for cloud-free conditions is lower. This can also difficult the differentiation of clouds with respect to a cloud-free back-ground with high aerosol load. The sky radiances at angles where a cloud is viewed (cloud-contaminated) are usually identified using cloud-screening algorithms, like the one from AERONET, which evaluates the differences between symmetric sky radiances. This criterion has been applied to the simulated sky radiances to detect the CEF corresponding to cloud-contaminated scattering angles, and have been labeled with cross markers in the bottom panels of Fig. 5. As it was expected, some cloud-contaminated data are not correctly identified when the AOD increases. This effect is primarily observed at 440 nm due to the higher

background sky radiance at this wavelength under cloud-free condi-tions; i.e. for scattering angles between 50 and 100° in Fig. 5g and h. The cloud-screening used is applied separately for each wavelength, because
real measurements are not instantaneously recorded for all the wave-lengths and, therefore, these contaminated measurements may be included in the retrieval.

The CEF has been averaged over the four types of aerosol for each partially cloudy scenario and aerosol load to obtain a more represen-tative result of each scenario for all aerosol types, since they show a similar behaviour. The averaged CEF values and their standard devia-tion (error bars) are shown in Fig. 6 for the nine partially cloudy sce-narios when AOD_{440} is 0.2. In this figure, the CEF values corresponding to sky radiances identified as cloud-contaminated have not been included. Unlike in Fig. 5, where there are very high CEF values corre-sponding to the clouds, in Fig. 6 it can be clearly appreciated the effect of clouds only in the sky radiances that pass the cloud-screening criterion. Fig. 6 points out that higher CEF values appear for high scattering angles and they are higher at longer wavelengths, except for scattering

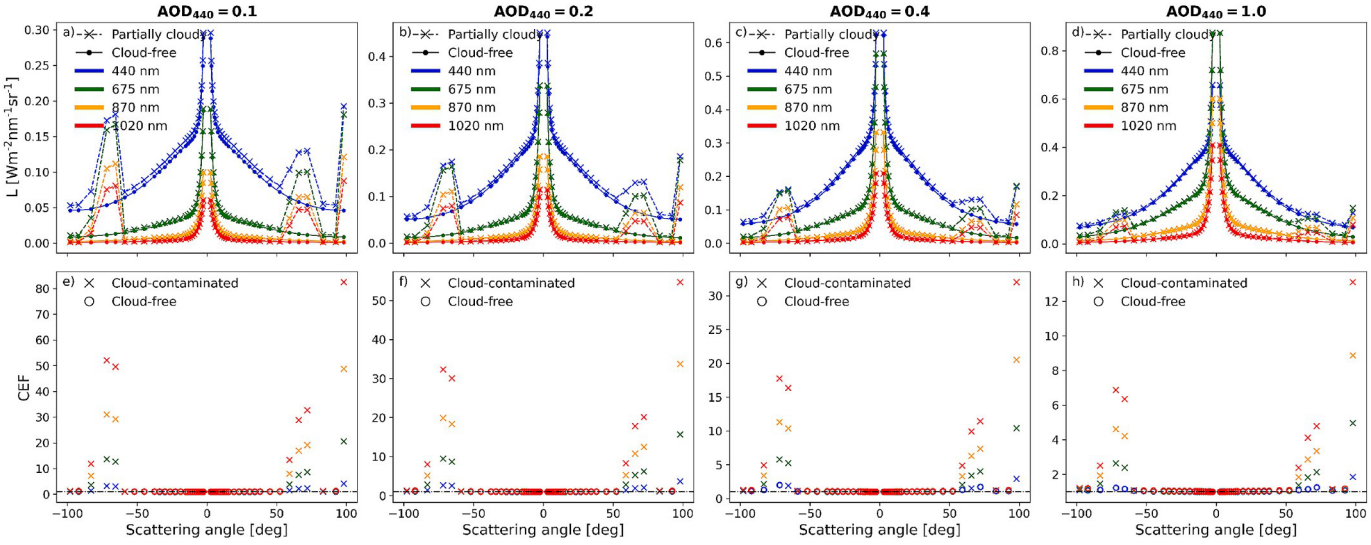

Fig. 5. Sky radiances (L) in the almucantar geometry simulated with MYSTIC for the ZAMB aerosol type in cloud-free conditions (circle marker) and partially cloudy conditions (Cloud cover C with SZA = 50° and SAA = 50°) (cross marker) and the corresponding CEFs at 440, 675, 870 and 1020 nm for AOD at 440 nm (AOD_{440}) equal to 0.1 (a,e), 0.2 (b,f), 0.4 (c,g) and 1.0 (d,h). The CEF values corresponding to the scattering angles at which the sky radiances do not pass the cloud-screening are marked with a cross and those that do pass with an empty circle.

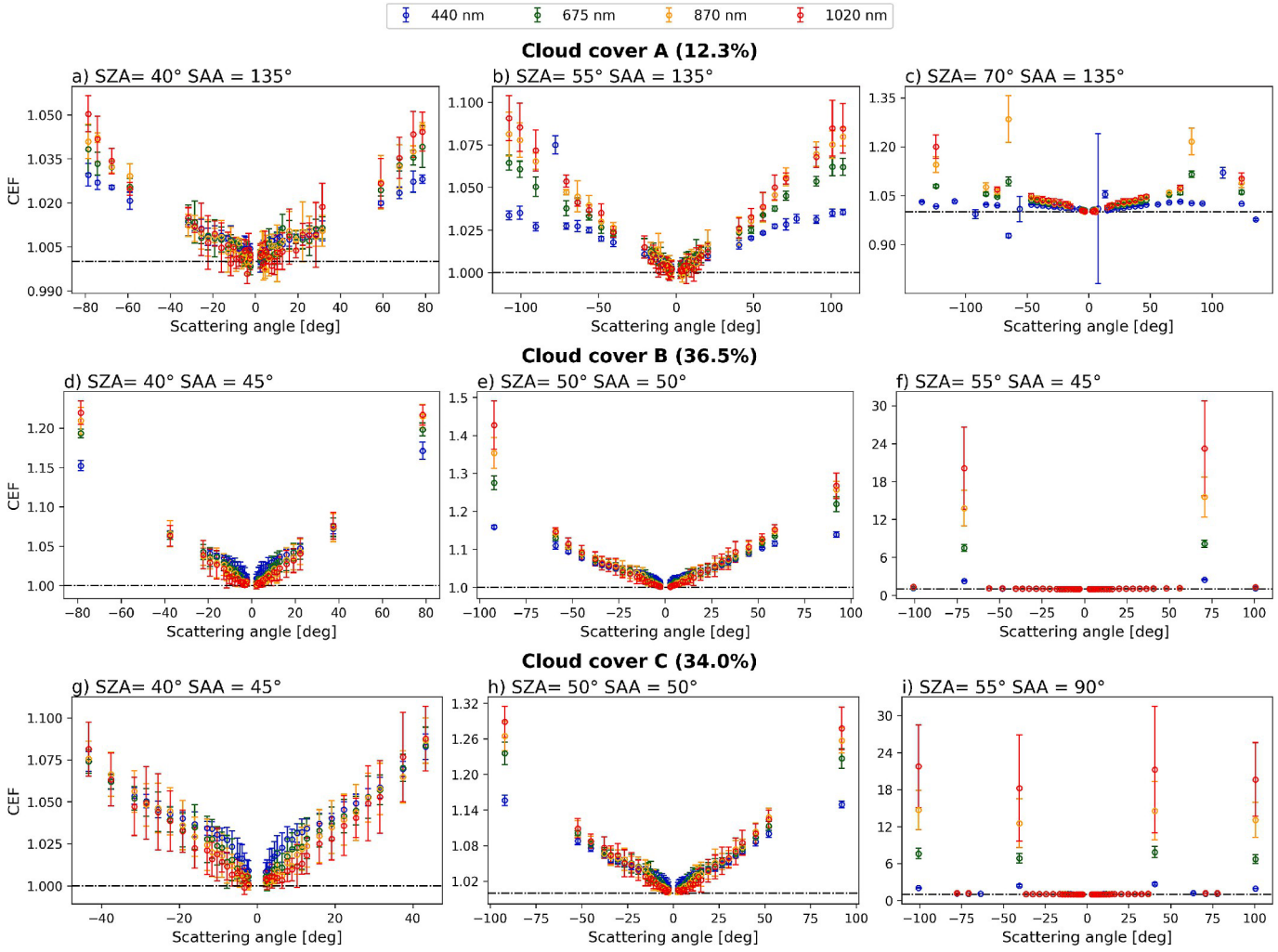

Fig. 6. Error bar plots of the mean cloud enhancement factor (CEF) for AOD at 440 nm (AOD_{440}) of 0.2 calculated averaging the CEF of the four aerosol types for each cloud cover as a function of the scattering angle. The error bars represent the standard deviation of the average. Only the scattering angles that satisfy the cloud-screening criterion have been plotted.

angles close to the solar aureole. This behaviour in the aureole is mainly due to aerosols, because their scattering is stronger at shorter scattering angles (e.g., see Fig. S5 of Roman et al., 2022b), specially for coarse particles, causing higher cloud-free sky radiances and, hence, lower CEF values at these angles. It also explains the different spectral behaviour of the CEF with the scattering angle since the lower angles are dominated by aerosol scattering, with lower spectral dependence, and the higher ones are dominated by Rayleigh scattering, with a higher spectral dependence that increase the CEF values at longer wavelengths. Fig. S1 included in the supplementary material, which is similar to Fig. 6 but considering a pure Rayleigh cloud-free atmosphere (AOD = 0), corroborates this explanation: if there are no aerosols then the CEF values are higher, with a lower dependence on scattering angle, and always higher for longer wavelengths. This was expected because the Rayleigh scat-tering is stronger for shorter wavelengths and its variation with scat-tering angle is lower than in the Mie scattering from aerosols. In addition, the significant asymmetries on the CEF values with respect to the scattering angle observed in Fig. S1 (e.g. in Cloud cover C with SZA = 50° and SAA = 50° Fig. 2h), reveal that the enhancement caused by clouds could also depend on the cloud positions regarding the observed sky point, with higher enhancements closer to the clouds.

To characterize each partially cloudy scenario, the mean and median CEF values at each wavelength have been calculated considering all the scattering angles that pass the cloud-screening criterion. These values have been also collected in Table 2 for each partially cloudy scenario and AOD. For all the scenarios it is observed that the median CEF values decrease with the AOD, which is more evident at shorter wavelengths. For higher aerosol load, the sky radiance increases and therefore the ratio between cloud-free and cloudy conditions is smaller. In contrast, the mean values generally increase with the AOD. The cloud-screening exhibits a worse performance for higher aerosol loads and therefore some cloud-contaminated points are not correctly identified and introduced in the average. The Cloud cover A (12.3 % of cloud fraction) is in general the one that presents the lower cloud impact in the sky radiances, which presents a median enhancement of about 0–3 %. For the Cloud cover B (36.5 % of cloud fraction) and C (34.0 % of cloud fraction) a higher enhancement is observed, with median values of about 1–5 %. These values are strongly influenced by the low values observed at the scattering angles from the solar aureole, where there are more points, but it can be clearly seen (Fig. 6) that the CEF values are higher for longer scattering angles in Cloud cover B and C, with enhancements around 10–20 %. Some extreme values appear for the means due to cloud-contaminated points, specially for the Cloud cover B with SZA = 55° and SAA = 45° (Fig. 2f) and the Cloud cover C with SZA = 55° and SAA = 90° (Fig. 2i), where there are symmetric points with clouds which are not efficiently filtered. This could be partially caused by the artificial cloud scene, where likely the clouds are more similar than in reality.

Table 2
Mean (an median in parenthesis) cloud enhancement factor (CEF) values at wavelengths (λ) of 440, 675, 870 and 1020 nm for each partially cloudy scenario (three Sun positions for each of the three cloud covers) for AOD at 440 nm equal to 0.1, 0.2, 0.4 and 1.0. Only the CEFs corresponding to sky radiances identified as cloud-free with the cloud-screening have been considered in the average.

	Cloud cover A											
	SZA = 40° SAA =				SZA = 55° SAA =				SZA = 70° SAA =			
AOD (440 nm)	λ (440 *nm*)	λ (675 *nm*)	λ (870 *nm*)	λ (1020 *nm*)	λ (440 *nm*)	λ (675 *nm*)	λ (870 *nm*)	λ (1020 *nm*)	λ (440 *nm*)	λ (675 *nm*)	λ (870 *nm*)	λ (1020 *nm*)
0.1	1.012 (1.009)	1.013 (1.008)	1.013 (1.007)	1.012 (1.004)	1.019 (1.012)	1.024 (1.017)	1.026 (1.014)	1.027 (1.012)	1.028 (1.020)	1.039 (1.027)	1.034 (1.030)	1.038 (1.027)
0.2	1.010 (1.008)	1.010 (1.007)	1.011 (1.006)	1.011 (1.004)	1.016 (1.010)	1.020 (1.011)	1.024 (1.011)	1.024 (1.008)	1.015 (1.013)	1.030 (1.023)	1.045 (1.026)	1.033 (1.026)
0.4	1.038 (1.005)	1.008 (1.004)	1.009 (1.005)	1.009 (1.004)	1.015 (1.008)	1.021 (1.008)	1.019 (1.008)	1.021 (1.008)	1.006 (1.009)	1.026 (1.016)	1.035 (1.020)	1.037 (1.023)
1.0	1.022 (1.004)	1.037 (1.003)	1.007 (1.003)	1.008 (1.004)	1.009 (1.005)	1.021 (1.007)	1.018 (1.006)	1.021 (1.008)	0.998 (1.008)	1.020 (1.011)	1.020 (1.012)	1.020 (1.014)
	Cloud cover B											
	SZA ¼ 40° SAA ¼				**SZA ¼ 50° SAA ¼**				**SZA ¼ 55° SAA ¼**			
AOD (440 nm)	λ (440 *nm*)	λ (675 *nm*)	λ (870 *nm*)	λ (1020 *nm*)	λ (440 *nm*)	λ (675 *nm*)	λ (870 *nm*)	λ (1020 *nm*)	λ (440 *nm*)	λ (675 *nm*)	λ (870 *nm*)	λ (1020 *nm*)
0.1	1.049 (1.043)	1.042 (1.028)	1.037 (1.017)	1.033 (1.011)	1.062 (1.052)	1.066 (1.050)	1.066 (1.039)	1.065 (1.034)	1.140 (1.053)	1.546 (1.055)	2.125 (1.046)	2.742 (1.038)
0.2	1.037 (1.029)	1.033 (1.022)	1.030 (1.014)	1.029 (1.012)	1.049 (1.038)	1.053 (1.035)	1.055 (1.035)	1.055 (1.028)	1.108 (1.041)	1.362 (1.042)	1.674 (1.039)	1.992 (1.034)
0.4	1.068 (1.021)	1.026 (1.016)	1.026 (1.015)	1.027 (1.013)	1.038 (1.027)	1.043 (1.027)	1.047 (1.027)	1.048 (1.025)	1.074 (1.029)	1.210 (1.031)	1.361 (1.033)	1.513 (1.028)
1.0	1.070 (1.021)	1.062 (1.013)	1.021 (1.012)	1.022 (1.011)	1.049 (1.023)	1.033 (1.020)	1.037 (1.022)	1.039 (1.022)	1.054 (1.024)	1.084 (1.023)	1.134 (1.024)	1.183 (1.026)
	Cloud cover C											
	SZA ¼ 40° SAA ¼				**SZA ¼ 50° SAA ¼**				**SZA ¼ 55° SAA ¼**			
AOD (440 nm)	λ (440 *nm*)	λ (675 *nm*)	λ (870 *nm*)	λ (1020 *nm*)	λ (440 *nm*)	λ (675 *nm*)	λ (870 *nm*)	λ (1020 *nm*)	λ (440 *nm*)	λ (675 *nm*)	λ (870 *nm*)	λ (1020 *nm*)
0.1	1.046 (1.045)	1.039 (1.035)	1.034 (1.026)	1.029 (1.017)	1.058 (1.050)	1.059 (1.046)	1.057 (1.036)	1.053 (1.027)	1.219 (1.052)	1.992 (1.051)	3.112 (1.043)	4.252 (1.031)
0.2	1.034 (1.032)	1.029 (1.024)	1.027 (1.020)	1.025 (1.015)	1.045 (1.037)	1.048 (1.036)	1.048 (1.031)	1.047 (1.023)	1.158 (1.038)	1.638 (1.037)	2.253 (1.033)	2.871 (1.031)
0.4	1.031 (1.021)	1.022 (1.019)	1.023 (1.018)	1.022 (1.014)	1.085 (1.028)	1.038 (1.025)	1.041 (1.025)	1.042 (1.021)	1.101 (1.031)	1.359 (1.027)	1.659 (1.028)	1.963 (1.026)
1.0	1.039 (1.016)	1.024 (1.015)	1.018 (1.014)	1.019 (1.014)	1.057 (1.021)	1.089 (1.019)	1.033 (1.020)	1.035 (1.020)	1.046 (1.023)	1.126 (1.024)	1.227 (1.024)	1.327 (1.023)

3.3. Retrieval of aerosol properties under partially cloudy scenarios

Once determined the CEF for each scenario, in this subsection we have studied the impact of this sky radiance enhancement on the retrieval of aerosol properties under partially cloudy conditions. To this end, we have used the set of synthetic observations (sky radiances, AOD and RCS) generated with the RTMs (see Section 2.4) for 8 × 16 cloud-aerosol scenarios; the Cloud cover C with SZA = 40° and SAA = 45° scenario has been discarded since it does not present enough scattering angles to pass the quality assurance criterion detailed in 2.1.1 (see Fig. 6) for any aerosol scenario. Only the N-convergent aerosol properties retrieved by GRASP$_{pac}$ for these observations (200 for each partially cloudy/cloud-free scenario, minus those rejected by the cloud-screening criteria) have been averaged to obtain the mean aerosol properties for each clouds-aerosol scenario together with their standard deviation.

The analysis of the aerosol properties retrieved under partially cloudy scenarios has been divided into two parts. First, an analysis has been conducted using some particular cloudy scenarios: one with low and other with higher CEF values. Finally, an average analysis has been performed using only partially cloudy scenarios which show a clear impact of clouds, in order to estimate the bias introduced by their presence in the retrieved aerosol properties.

3.3.1. Individual cases of study: Weak and stronger sky radiance enhancement

The Cloud cover A with SZA = 55° and SAA = 135° (Fig. 2b) has been selected as a weak cloud impact scenario, since it presents median enhancements of 0.5–1.7 % (see Table 2).

The mean and standard deviations of the retrieved RRI, IRI, SSA, g and size distribution from the cloud-free and partially cloudy scenarios, but also the ones corresponding to the reference aerosol, have been plotted for the aerosol types ZAMB (fine), in Fig. 7, and SOLV (coarse), in Fig. S2 in the supplementary material. In both cases, the aerosol properties retrieved under the cloudy and the equivalent cloud-free conditions generally show a good correlation with the reference aerosol properties, especially for high AOD as expected (Holben et al., 2006). In the case of the RRI, SSA and g the presence of clouds shows some impact, as the values retrieved for these conditions are more separated from the reference values than those from cloud-free conditions. Nevertheless, as the shaded areas indicate, this difference is within the uncertainty of the retrieval for cloud-free conditions. The retrieved volume size distribution is similar in both retrievals; no significant differences are observed. The same plots for GSFC and LANA, included in Fig. S3 and S4 respectively in the supplementary material, show similar results than ZAMB and SOLV; we do not observe a clear dependence on type of aerosol.

For a quantitative analysis, the differences between the retrieved properties and the reference values have been calculated for each individual retrieval; i.e. the 200 (perturbed observations) x 16 (aerosol scenarios) retrievals that satisfy the quality criteria for the cloud-free and partially cloudy scenarios. The means and standard deviations of these differences for the partially cloudy and the equivalent cloud-free scenarios, calculated for each aerosol load and considering the retrievals from the four aerosol types, have been reported in Table 3. For the optical properties, the mean differences for both cloudy and cloud-free conditions decrease (in absolute value) for higher AODs, as expected; while these differences for the volume size distribution parameters do not show any clear dependence with AOD. For the optical properties, the precision (standard deviation) improves for higher AODs in both cloudy and cloud-free conditions, but for the volume size distribution parameters it remains similar for all AODs. In particular, for the SSA the precision decreases (the standard deviation increases) at longer wavelengths. For all the parameters, the standard deviations obtained in cloudy conditions are similar to the ones obtained in the cloud-free conditions, indicating that the precision of the retrieval is not related to the presence of clouds. However, there is a significant change

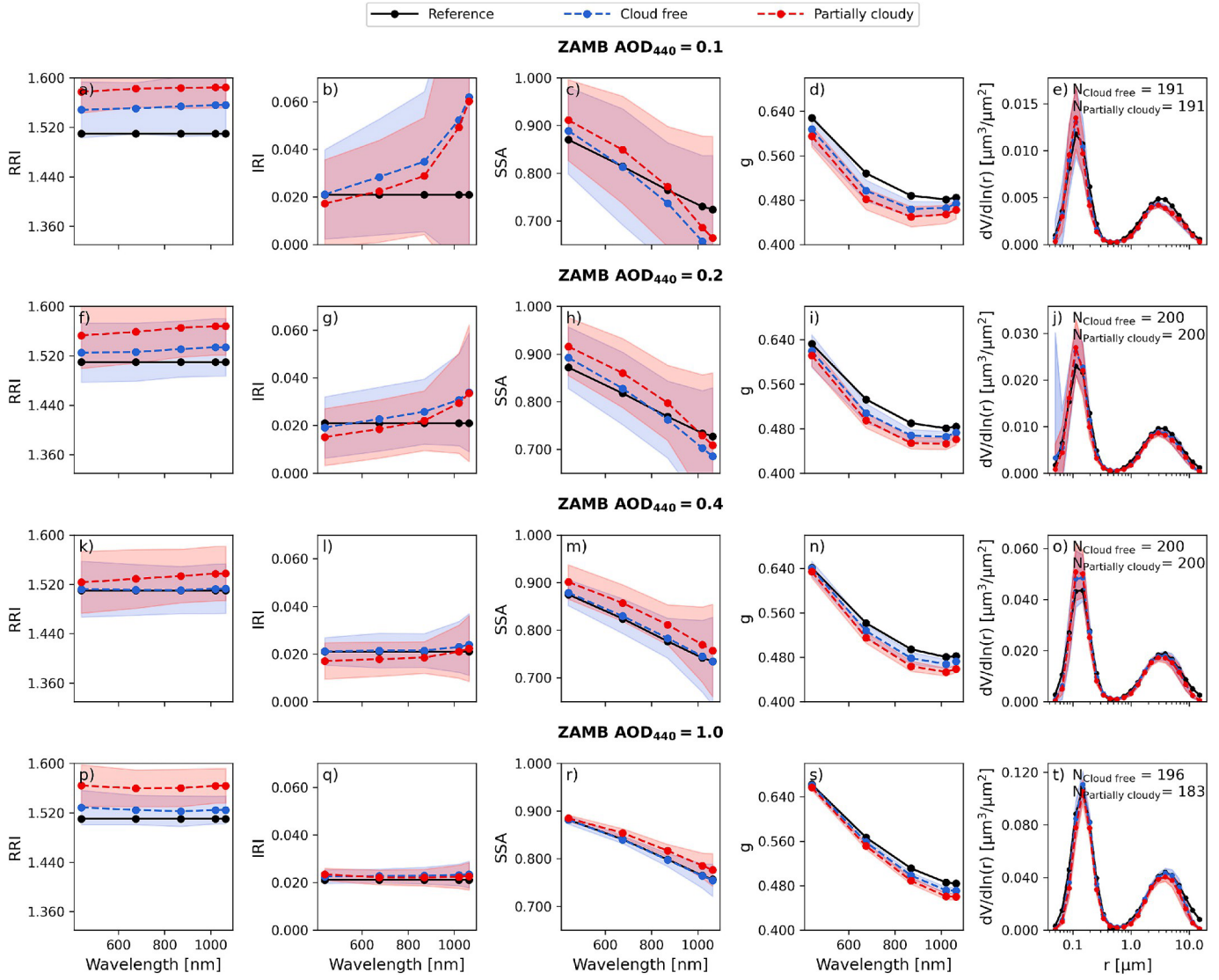

Fig. 7. Mean values of the retrieved aerosol properties under cloud-free (blue dashed line) and partially cloudy conditions (red dashed line) for the Cloud cover A with SZA = 55° and SAA = 135° for the ZAMB scenarios. Original properties are included as reference (black solid line). The shaded area represents the standard deviation of the properties for the cloud-free and partially cloudy scenarios. The number of available retrievals (N) used for the average for the cloud-free ($N_{Pcloud\text{-}free}$) and the partially cloudy ($N_{Partially\ cloudy}$) scenarios, at each AOD, have been included. Each column corresponds to one aerosol property; in order: real refractive index (RRI), imaginary refractive index (IRI), single scattering albedo (SSA), asymmetry factor (g) and volume size distribution (dV/dln(r)). Each row corresponds to the different values of AOD at 440 nm (AOD_{440}) values; in order, equal to 0.1, 0.2, 0.4 and 1.0. (For interpretation of the references to colour in this figure legend, the reader is referred to the web version of this article.)

in the mean differences that shows that, in the partially cloudy scenario, the overestimation and underestimation observed in the cloud-free conditions for the RRI and the g, respectively, are doubled. For AOD

at 440 nm equal to 0.4, the bias averaged for all wavelengths increases from 0.008 to 0.026 for the RRI, and from −0.006 to −0.016 for the g. The results for the volume size distribution are similar in both condi-

tions, probably because the retrieval of this property is mostly influ-enced by the AODs observations, which have not been affected by the presence of clouds (Torres et al., 2017).

The obtained values corroborate the low effect of the presence of clouds in the retrieval of aerosol properties observed in Fig. 7, S2, S3 and S4 for this partially cloudy scenario.

For the analysis of a stronger cloud impact scenario it has been selected the Cloud cover C with SZA = 50° and SAA = 50° (Fig. 2h), which presents median enhancements of 1.9–5 % (see Table 2). The average retrieved aerosol properties for ZAMB aerosol type, together with the reference values, have been represented in Fig. 8; the results for

SOLV, GSFC and LANA are included in Figs. S5, S6 and S7, respectively, in the supplementary material. For this scenarios, the distinction be-tween the results for cloudy and cloud-free conditions is more evident. The aerosol properties retrieved under cloud-free conditions closely correlate with the reference results, especially for the higher aerosol loads. On the other hand, the differences between the aerosol properties retrieved in cloudy conditions and the reference values are higher than the method's precision, since the shaded areas generally do not cover the reference values, specially for high AODs. In both ZAMB and SOLV, the SSA is always overestimated in the presence of clouds. This is explained by the fact that, for cloudy conditions, there is an enhance-ment effect (as shown in Fig. 6) and therefore more sky radiance is measured than under the expected cloud-free conditions, which is compensated in the retrieval by lower aerosol absorption. Consequently, this affects the other optical properties, which are less accurate than in the absence of clouds. For low AODs, the agreement for IRI and SSA (Figs. S5, S6 and S7) is occasionally a little bit better for the cloud

Table 3

Mean (and standard deviations in parenthesis) values of the differences between the aerosol properties retrieved in the inversion and the reference properties, for the partially cloudy scenario Cloud cover A with SZA = 55° and SAA = 135° and its corresponding cloud-free. These values have been calculated individually for AOD at 440 nm equal to 0.1, 0.2, 0.4 and 1.0., considering the available inversions from ZAMB, SOLV, GSFC and LANA. The optical properties, given at wavelengths (λ) of 440, 675, 870 and 1020 nm, are: the real refractive index (RRI), imaginary refractive index (IRI), single scattering albedo (SSA) and asymmetry factor (g). The volume size distribution is described by the bi-lognormal parameters for the fine and coarse modes: the volume median radius (r), standard deviation of log-normal distribution (σ) and aerosol volume concentration (VC).

		Cloud-free				Partially cloudy			
	AOD (440 nm)	λ (440 nm)	λ (675 nm)	λ (870 nm)	λ (1020 nm)	λ (440 nm)	λ (675 nm)	λ (870 nm)	λ (1020 nm)
RRI	0.1	0.0457 (0.0675)	0.0451 (0.0628)	0.0451 (0.0686)	0.0456 (0.0696)	0.0769 (0.0688)	0.0786 (0.0647)	0.0780 (0.0684)	0.0779 (0.0689)
	0.2	0.0233 (0.0538)	0.0224 (0.0475)	0.0248 (0.0489)	0.0252 (0.0512)	0.0476 (0.0604)	0.0495 (0.0532)	0.0532 (0.0547)	0.0537 (0.0568)
	0.4	0.0082 (0.0397)	0.0083 (0.0321)	0.0074 (0.0300)	0.0076 (0.0330)	0.0227 (0.0426)	0.0253 (0.0363)	0.0267 (0.0333)	0.0281 (0.0365)
	1.0	0.0094 (0.0247)	0.0074 (0.0192)	0.0058 (0.0196)	0.0059 (0.0200)	0.0256 (0.0324)	0.0223 (0.0284)	0.0217 (0.0289)	0.0229 (0.0301)
IRI	0.1	0.0037 (0.0125)	0.0051 (0.0140)	0.0074 (0.0171)	0.0136 (0.0330)	0.0011 (0.0115)	0.0022 (0.0120)	0.0044 (0.0141)	0.0109 (0.0344)
	0.2	0.0009 (0.0079)	0.0014 (0.0076)	0.0027 (0.0083)	0.0053 (0.0127)	−0.0014 (0.0073)	−0.0006 (0.0069)	0.0009 (0.0075)	0.0041 (0.0134)
	0.4	0.0002 (0.0035)	0.0001 (0.0040)	0.0003 (0.0039)	0.0013 (0.0061)	−0.0015 (0.0044)	−0.0015 (0.0039)	−0.0011 (0.0036)	0.0001 (0.0062)
	1.0	0.0003 (0.0018)	0.0004 (0.0017)	0.0005 (0.0020)	0.0006 (0.0027)	0.0003 (0.0019)	−0.0004 (0.0019)	−0.0004 (0.0020)	−0.0003 (0.0027)
SSA	0.1	−0.0193 (0.0780)	−0.0291 (0.0878)	−0.0430 (0.0934)	−0.0658 (0.1283)	0.0017 (0.0673)	−0.0032 (0.0778)	−0.0166 (0.0871)	−0.0392 (0.1262)
	0.2	−0.0020 (0.0536)	−0.0052 (0.0523)	−0.0152 (0.0582)	−0.0329 (0.0895)	0.0169 (0.0461)	0.0163 (0.0467)	0.0065 (0.0539)	−0.0138 (0.0887)
	0.4	0.0027 (0.0273)	0.0023 (0.0262)	0.0009 (0.0289)	−0.0069 (0.0520)	0.0169 (0.0273)	0.0199 (0.0240)	0.0186 (0.0274)	0.0101 (0.0515)
	1.0	0.0015 (0.0107)	−0.0003 (0.0080)	0.0002 (0.0107)	0.0002 (0.0179)	0.0057 (0.0102)	0.0122 (0.0085)	0.0146 (0.0107)	0.0152 (0.0173)
g	0.1	−0.0192 (0.0272)	−0.0101 (0.0228)	−0.0020 (0.0196)	0.0013 (0.0177)	−0.0345 (0.0238)	−0.0277 (0.0237)	−0.0182 (0.0206)	−0.0139 (0.0175)
	0.2	−0.0123 (0.0236)	−0.0090 (0.0163)	−0.0059 (0.0132)	−0.0032 (0.0112)	−0.0231 (0.0201)	−0.0223 (0.0159)	−0.0192 (0.0142)	−0.0158 (0.0117)
	0.4	−0.0070 (0.0202)	−0.0066 (0.0110)	−0.0059 (0.0103)	−0.0050 (0.0080)	−0.0133 (0.0195)	−0.0169 (0.0112)	−0.0176 (0.0116)	−0.0170 (0.0093)
	1.0	−0.0049 (0.0113)	−0.0037 (0.0062)	−0.0043 (0.0079)	−0.0052 (0.0075)	−0.0079 (0.0109)	−0.0077 (0.0075)	−0.0098 (0.0101)	−0.0118 (0.0105)
		fine		coarse		fine		coarse	
$r[\mu m]$	0.1	0.0034 (0.0106)		−0.0982 (0.1308)		−0.0014 (0.0093)		−0.1145 (0.1306)	
	0.2	0.0039 (0.0099)		−0.1341 (0.1261)		0.0010 (0.0085)		−0.1517 (0.1215)	
	0.4	0.0047 (0.0112)		−0.1397 (0.1459)		0.0033 (0.0116)		−0.1547 (0.1470)	
	1.0	0.0049 (0.0100)		−0.1575 (0.2321)		0.0056 (0.0108)		−0.1610 (0.2231)	
$\sigma[\mu m]$	0.1	0.0114 (0.0440)		−0.0356 (0.0576)		0.0024 (0.0430)		−0.0296 (0.0509)	
	0.2	−0.0038 (0.0421)		−0.0658 (0.0553)		−0.0120 (0.0457)		−0.0617 (0.0517)	
	0.4	−0.0009 (0.0529)		−0.0790 (0.0524)		−0.0130 (0.0583)		−0.0778 (0.0494)	
	1.0	0.0261 (0.0687)		−0.1058 (0.0553)		0.0226 (0.0727)		−0.1065 (0.0570)	
$VC[\mu m^3/\mu m^2]$	0.1	−0.0012 (0.0045)		−0.0011 (0.0024)		−0.0017 (0.0045)		−0.0017 (0.0021)	
	0.2	−0.0014 (0.0078)		−0.0021 (0.0048)		−0.0026 (0.0070)		−0.0032 (0.0046)	
	0.4	−0.0005 (0.0087)		−0.0041 (0.0080)		−0.0022 (0.0091)		−0.0056 (0.0080)	
	1.0	−0.0010 (0.0124)		−0.0155 (0.0195)		−0.0063 (0.0140)		−0.0190 (0.0200)	

contaminated measurements, but the shaded areas mainly overlaps for both retrievals. This is because the sunlight scattered by aerosols is lower for low aerosol concentration and therefore it gives few infor-

mation for the retrieval, presenting a less accurate result. For example, AERONET requires AOD at 440 nm > 0.4 to consider the retrieved SSA as quality assurance product (level 2.0 data; Sinyuk et al., 2020). Then,

the observed results can be explained because the uncertainty in the aerosol retrievals is higher for low aerosol loads, and both retrievals are within this uncertainty. The volume size distribution still shows a very good agreement both in the cloudy and cloud-free conditions, in consistence with the previous reasoning about the influence of the AOD values on the retrieval of this property.

This behaviour is similar for all the aerosol types, therefore the average for the quantitative analysis can be conducted again without differentiation

between aerosol types. The mean and standard de-viations of the differences between the retrieved and the reference aerosol properties for this scenario are collected in Table 4. As expected, the mean differences for the cloud-free conditions are very similar to the ones obtained in the previous scenario (see Table 3). With respect to the cloudy conditions, the mean differences for the optical properties again decrease for higher AODs. However, in this case, this dependence is less evident, especially for the highest AODs. In general, for the optical properties, these differences are higher (in absolute value) than the ones showed in Table 3 for the previous scenario; this increase is not so evident for the volume size distribution parameters. The corresponding standard deviations are similar to those from Table 3, confirming that the presence of clouds does not affect the precision of the inversion strategy, but it does affect the accuracy, introducing a bias in some of the retrieved properties, which are systematically overestimated or under-estimated. In this situation, the RRI and the g are again the most over-estimated and underestimated properties, respectively, but now the bias observed in the cloud-free conditions is usually more than doubled in the partially cloudy conditions, with the highest change observed for higher AOD. For AOD at 440 nm equal to 0.4, the bias averaged for all wavelengths is now 0.070 compared to 0.026 in the previous scenario for the RRI, and − 0.032 instead of −0.016 for the g. With respect to the size distribution parameters, those corresponding to the coarse mode are now slightly more underestimated, especially for the volume concen-tration, than in Table 3. This effect is also seen for the volume concen-tration of the fine mode, but any clear pattern is yet observed for the median radius and standard deviation of this mode.

3.3.2. Average cloud impact

It has been seen in the previous subsection that the partially cloudy scenarios with low CEF do not introduce a strong impact in the retrieved aerosol properties. In order to estimate the average effect in the retrieval of aerosol properties of scenarios that present a significant CEF, all the retrievals from the five partially cloudy scenarios corresponding to the Cloud cover B and C, which present median enhancements between 1 and 5 %, have been averaged for aerosol type and load. The presence of symmetric points viewing clouds in the Cloud cover B with SZA = 55° and SAA = 45° (Fig. 2f) and in the Cloud cover C with SZA = 55° and SAA = 90° (Fig. 2i) scenarios, which are not efficiently removed by the cloud-screening (see Fig. 6), complicates the retrieval, giving high values of the residual. Therefore the convergence quality assurance criterion rejects all the retrievals from these partially cloudy scenarios, excluding them from the average analysis. The mean properties ob-tained for the partially cloudy scenarios and their corresponding cloud-free scenarios, together with the reference values, for ZAMB, SOLV, GSFC and LANA have been represented in Figs. S8, S9, S10 and S11 in the supplementary material, respectively. As expected, these figures are very similar to Fig. 8, S5, S6 and S7 obtained in the previous section for the stronger cloud impact analysis, showing a clear impact of the pres-ence of clouds on the retrieval of aerosol properties in these cloudy conditions.

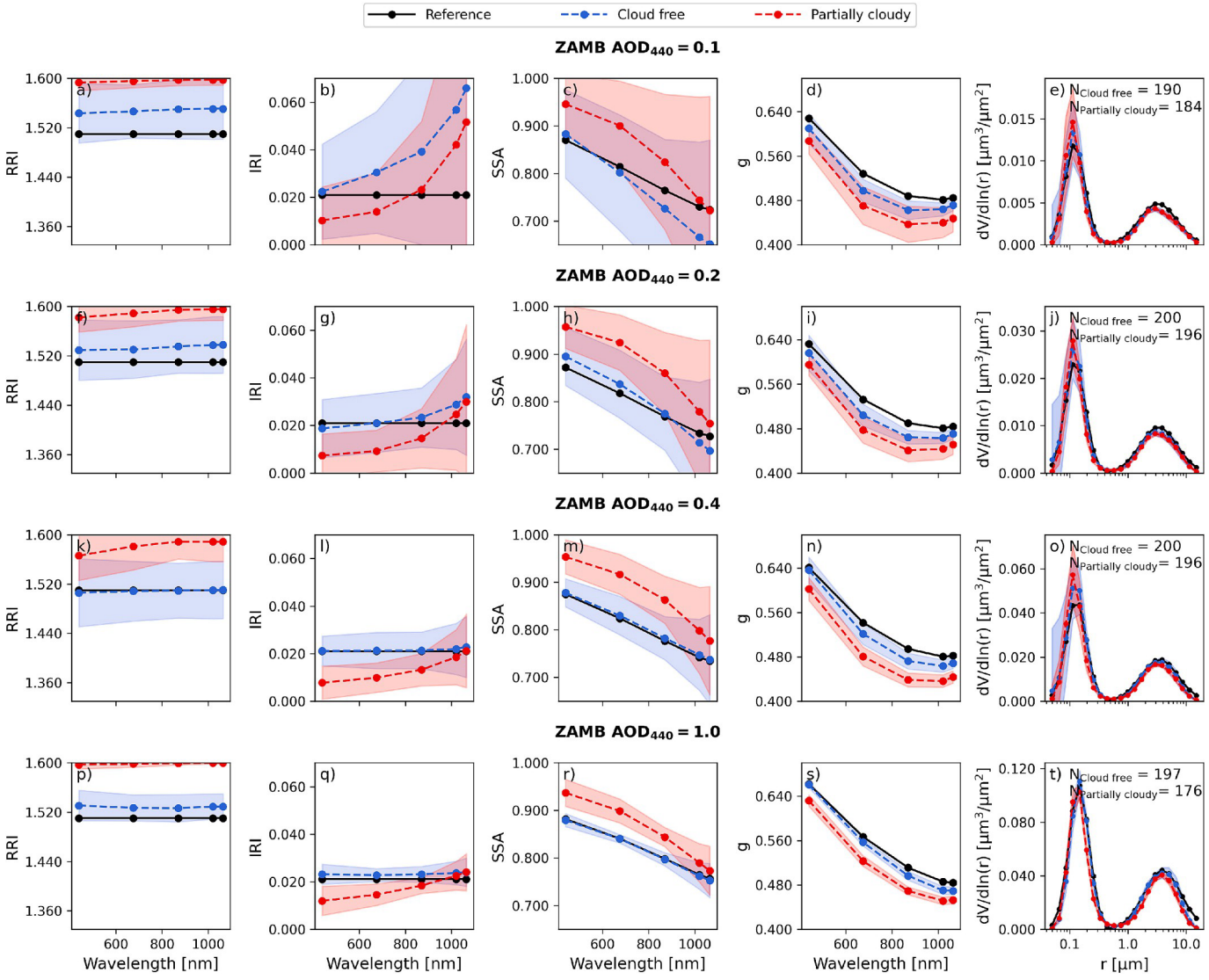

Fig. 8. Mean values of the retrieved aerosol properties under cloud-free (blue dashed line) and partially cloudy conditions (red dashed line) for the Cloud cover C with SZA = 50° and SAA = 50° for the ZAMB scenarios. Original properties are included as reference (black solid line). The shaded area represents the standard deviation of the properties for the cloud-free and partially cloudy scenarios. The number of available retrievals (N) used for the average for the cloud-free ($N_{Cloud\ free}$) and the partially cloudy ($N_{Partially\ cloudy}$) scenarios, at each AOD, have been included. Each column corresponds to one aerosol property; in order: real refractive index (RRI), imaginary refractive index (IRI), single scattering albedo (SSA), asymmetry factor (g) and volume size distribution (dV/dln(r)). Each row corresponds to the different values of AOD at 440 nm (AOD_{440}) values; in order, equal to 0.1, 0.2, 0.4 and 1.0. (For interpretation of the references to colour in this figure legend, the reader is referred to the web version of this article.)

Table 4. Mean (and standard deviations in parenthesis) values of the differences between the aerosol properties retrieved in the inversion and the reference properties, for the partially cloudy scenario Cloud cover C with SZA = 50° and SAA = 50° and its corresponding cloud-free. These values have been calculated individually for AOD at 440 nm equal to 0.1, 0.2, 0.4 and 1.0., considering the available inversions from ZAMB, SOLV, GSFC and LANA. The optical properties, given at wavelengths (λ) of 440,
675, 870 and 1020 nm, are: the real refractive index (RRI), imaginary refractive index (IRI), single scattering albedo (SSA) and asymmetry factor (g). The volume size distribution is described by the bi-lognormal parameters for the fine and coarse modes: the volume median radius (r), standard deviation of log-normal distribution (σ) and aerosol volume concentration (VC).

		Cloud-free				Partially cloudy			
	AOD (440 nm)	λ (440 nm)	λ (675 nm)	λ (870 nm)	λ (1020 nm)	λ (440 nm)	λ (675 nm)	λ (870 nm)	λ (1020 nm)
RRI	0.1	0.0459 (0.0687)	0.0452 (0.0636)	0.0456 (0.0688)	0.0458 (0.0699)	0.0994 (0.0694)	0.0988 (0.0683)	0.1001 (0.0701)	0.1002 (0.0704)
	0.2	0.0229 (0.0537)	0.0224 (0.0468)	0.0246 (0.0465)	0.0250 (0.0493)	0.0770 (0.0570)	0.0763 (0.0539)	0.0805 (0.0556)	0.0810 (0.0570)
	0.4	0.0052 (0.0419)	0.0064 (0.0346)	0.0063 (0.0320)	0.0058 (0.0346)	0.0669 (0.0486)	0.0679 (0.0420)	0.0713 (0.0387)	0.0719 (0.0433)
	1.0	0.0110 (0.0246)	0.0082 (0.0190)	0.0073 (0.0195)	0.0083 (0.0205)	0.0816 (0.0317)	0.0785 (0.0283)	0.0783 (0.0272)	0.0791 (0.0286)
IRI	0.1	0.0042 (0.0134)	0.0056 (0.0148)	0.0084 (0.0218)	0.0150 (0.0407)	−0.0030 (0.0088)	−0.0018 (0.0092)	0.0013 (0.0150)	0.0072 (0.0322)
	0.2	0.0005 (0.0075)	0.0009 (0.0071)	0.0019 (0.0075)	0.0043 (0.0118)	−0.0046 (0.0070)	−0.0038 (0.0066)	−0.0020 (0.0075)	0.0014 (0.0132)
	0.4	0.0002 (0.0037)	0.0001 (0.0041)	0.0003 (0.0042)	0.0011 (0.0065)	−0.0048 (0.0061)	−0.0039 (0.0053)	−0.0029 (0.0045)	−0.0009 (0.0067)
	1.0	0.0005 (0.0026)	0.0004 (0.0017)	0.0006 (0.0020)	0.0008 (0.0030)	−0.0036 (0.0044)	−0.0027 (0.0032)	−0.0017 (0.0019)	−0.0006 (0.0033)
SSA	0.1	−0.0208 (0.0800)	−0.0324 (0.0864)	−0.0470 (0.0984)	−0.0668 (0.1359)	0.0304 (0.0470)	0.0305 (0.0629)	0.0166 (0.0864)	−0.0039 (0.1277)
	0.2	−0.0002 (0.0511)	−0.0017 (0.0514)	−0.0099 (0.0574)	−0.0264 (0.0895)	0.0409 (0.0377)	0.0438 (0.0483)	0.0366 (0.0587)	0.0192 (0.0887)
	0.4	0.0011 (0.0278)	0.0024 (0.0275)	0.0004 (0.0308)	−0.0074 (0.0555)	0.0428 (0.0321)	0.0417 (0.0369)	0.0390 (0.0387)	0.0263 (0.0576)
	1.0	0.0012 (0.0131)	0.0003 (0.0082)	0.0000 (0.0107)	−0.0011 (0.0193)	0.0358 (0.0237)	0.0313 (0.0197)	0.0272 (0.0155)	0.0222 (0.0218)
g	0.1	−0.0200 (0.0285)	−0.0108 (0.0245)	−0.0027 (0.0214)	0.0010 (0.0192)	−0.0356 (0.0280)	−0.0316 (0.0376)	−0.0286 (0.0326)	−0.0280 (0.0278)
	0.2	−0.0124 (0.0244)	−0.0099 (0.0183)	−0.0070 (0.0147)	−0.0042 (0.0120)	−0.0302 (0.0191)	−0.0280 (0.0266)	−0.0262 (0.0229)	−0.0249 (0.0186)
	0.4	−0.0067 (0.0207)	−0.0079 (0.0147)	−0.0075 (0.0132)	−0.0064 (0.0100)	−0.0362 (0.0184)	−0.0336 (0.0207)	−0.0303 (0.0191)	−0.0275 (0.0142)
	1.0	−0.0045 (0.0115)	−0.0037 (0.0069)	−0.0046 (0.0094)	−0.0058 (0.0087)	−0.0351 (0.0115)	−0.0345 (0.0130)	−0.0330 (0.0111)	−0.0315 (0.0083)
		fine		coarse		fine		coarse	
$r[\mu m]$	0.1	0.0030 (0.0115)		−0.0869 (0.1294)		0.0049 (0.0145)		−0.1101 (0.1206)	
	0.2	0.0040 (0.0104)		−0.1129 (0.1119)		0.0045 (0.0097)		−0.1517 (0.0919)	
	0.4	0.0050 (0.0120)		−0.1233 (0.1379)		−0.0012 (0.0114)		−0.1722 (0.1041)	
	1.0	0.0054 (0.0105)		−0.1231 (0.2276)		−0.0005 (0.0150)		−0.2509 (0.2012)	
$\sigma[\mu m]$	0.1	0.0114 (0.0472)		−0.0319 (0.0562)		0.0009 (0.0486)		−0.0373 (0.0476)	
	0.2	−0.0040 (0.0425)		−0.0652 (0.0512)		−0.0037 (0.0487)		−0.0709 (0.0438)	
	0.4	−0.0004 (0.0506)		−0.0802 (0.0502)		0.0056 (0.0576)		−0.0909 (0.0476)	
	1.0	0.0261 (0.0739)		−0.1042 (0.0561)		0.0326 (0.0861)		−0.1139 (0.0501)	
$VC[\mu m^3/\mu m^2]$	0.1	−0.0012 (0.0046)		−0.0009 (0.0024)		−0.0024 (0.0042)		−0.0023 (0.0021)	
	0.2	−0.0012 (0.0070)		−0.0021 (0.0045)		−0.0046 (0.0063)		−0.0048 (0.0043)	
	0.4	0.0011 (0.0141)		−0.0046 (0.0076)		−0.0056 (0.0115)		−0.0100 (0.0081)	
	1.0	−0.0015 (0.0127)		−0.0135 (0.0176)		−0.0205 (0.0174)		−0.0362 (0.0251)	

In order to quantify the bias introduced in the retrieved aerosol properties due to a significant enhancement of sky radiances under partially cloudy scenarios, the differences between the mean values retrieved under cloudy (Cloud cover B and C) and cloud-free conditions have been calculated and shown in Table 5. The presence of clouds introduces a positive bias in the retrieved RRI values of about 0.05, which slightly increases with AOD to almost 0.06 for extreme aerosol loads. This effect does not vary significantly with the wavelength. On the other hand, the IRI is underestimated due to the enhancement of the radiances; this underestimation tends to be greater for shorter wavelengths and lower AOD values. Clouds also induce a positive bias in the retrieved SSA values of 0.05–0.06 for low AOD values; this bias is reduced up to around 0.03 when the AOD_{440} increases to 1.0. These results indicate a significant underestimation of the aerosol absorption due to the enhancement of sky radiance caused by clouds. This cloud effect also leads to an underestimation between −0.015 and − 0.027 in the asymmetry factor for all wavelengths and aerosol loads. The differences between the cloud-free retrievals and the reference values are also included in Table 5, highlighting the loss of accuracy in all the retrieved optical properties when the retrieval is performed under cloudy conditions. Regarding the size distribution parameters, very small bias values are obtained under cloudy conditions, generally slightly increasing (in absolute value) the bias for cloud-free conditions (included in parenthesis), especially for the volume concentration. The effect of clouds in the retrieved volume size distribution parameters is not very significant, since the differences obtained are very small and usually smaller than the bias for cloud-free conditions (in parenthesis).

Table 5. Differences between the mean values retrieved under cloudy (significant Cloud cover B and C) and cloud-free conditions for different aerosol properties. The bias values of the mean cloud-free retrievals regards the reference values are in parenthesis. These values have been calculated individually for AOD at 440 nm equal to 0.1, 0.2, 0.4 and 1.0., considering the available inversions from ZAMB, SOLV, GSFC and LANA. The optical properties, given at wavelengths (λ) equal to 440, 675, 870 and 1020 nm, are: the real refractive index (RRI), imaginary refractive index (IRI), single scattering albedo (SSA) and asymmetry factor (g). The volume size distribution is described by the bi-lognormal parameters for the fine and coarse modes: the volume median radius (r), standard deviation of log-normal distribution (σ) and aerosol volume concentration (VC).

	AOD (440 nm)	λ (440 *nm*)	λ (675 *nm*)	λ (870 *nm*)	λ (1020 *nm*)
RRI	0.1	0.0526 (0.0403)	0.0526 (0.1013)	0.0530 (0.0530)	0.0530 (−0.0005)
	0.2	0.0522 (0.0236)	0.0515 (0.0576)	0.0532 (0.0180)	0.0537 (−0.0050)
	0.4	0.0527 (0.0038)	0.0533 (0.0200)	0.0564 (0.0075)	0.0578 (0.0016)
	1.0	0.0588 (0.0230)	0.0578 (0.0111)	0.0590 (0.0164)	0.0593 (−0.0018)
IRI	0.1	−0.0067 (0.0196)	−0.0065 (0.0113)	−0.0060 (0.0047)	−0.0063 (0.0041)
	0.2	−0.0050 (0.0041)	−0.0046 (0.0048)	−0.0039 (0.0016)	−0.0029 (0.0008)
	0.4	−0.0046 (0.0005)	−0.0037 (0.0013)	−0.0030 (0.0004)	−0.0019 (0.0001)
	1.0	−0.0035 (0.0019)	−0.0027 (0.0001)	−0.0021 (0.0001)	−0.0014 (0.0001)
SSA	0.1	0.0479 (−0.0351)	0.0576 (−0.0725)	0.0566 (−0.0439)	0.0566 (−0.0408)
	0.2	0.0408 (0.0005)	0.0458 (−0.0336)	0.0461 (−0.0177)	0.0446 (−0.0092)
	0.4	0.0384 (0.0068)	0.0374 (−0.0087)	0.0368 (−0.0045)	0.0318 (−0.0005)
	1.0	0.0321 (0.0017)	0.0287 (0.0004)	0.0259 (0.0007)	0.0228 (−0.0001)
g	0.1	−0.0154 (−0.0235)	−0.0206 (−0.0095)	−0.0248 (−0.0056)	−0.0274 (0.0089)
	0.2	−0.0170 (−0.0207)	−0.0182 (−0.0084)	−0.0193 (−0.0021)	−0.0205 (0.0006)
	0.4	−0.0232 (−0.0173)	−0.0229 (−0.0089)	−0.0217 (−0.0022)	−0.0209 (−0.0038)
	1.0	−0.0244 (−0.0145)	−0.0239 (−0.0068)	−0.0229 (−0.0032)	−0.0216 (−0.0014)
		fine		coarse	
$r[\mu m]$	0.1	0.0012 (0.0023)		−0.0223 (−0.0913)	
	0.2	0.0004 (0.0038)		−0.0293 (−0.1218)	
	0.4	−0.0035 (0.0037)		−0.0377 (−0.1234)	
	1.0	−0.0033 (0.0047)		−0.0805 (−0.1384)	
$\sigma[\mu m]$	0.1	−0.0113 (0.0112)		0.0016 (−0.0323)	
	0.2	−0.0053 (−0.0050)		−0.0006 (−0.0660)	
	0.4	−0.0031 (−0.0015)		−0.0048 (−0.0788)	
	1.0	0.0004 (0.0256)		−0.0059 (−0.1035)	
$VC[\mu m^3/\mu m^2]$	0.1	−0.0012 (−0.0011)		−0.0011 (−0.0010)	
	0.2	−0.0032 (−0.0011)		−0.0025 (−0.0023)	
	0.4	−0.0059 (0.0010)		−0.0052 (−0.0042)	
	1.0	−0.0164 (−0.0022)		−0.0135 (−0.0161)	

4. Conclusions

In this work we have analysed how the sky radiance is modified in the presence of clouds in comparison to the equivalent cloud-free situ-ation using the simulations run in the 3D radiative transfer model (RTM) MYSTIC from libRadtran. The sky radiance usually increases in all the points of the almucantar geometry used, even where there are not clouds located. This enhancement depends on the partially cloudy scenario. In the partially cloudy scenarios considered, it has been observed an enhancement with values generally between 0 and 20 %, being the major enhancement for cloud-free sky points close to clouds and for low scattering angles (close to the Sun). This enhancement is higher for longer wavelengths, except at the solar aureole due to aerosol scattering. The enhancement of sky radiance is much higher in points where there is a cloud located. Therefore, if the difference between the sky radiances in two symmetric points is very high (over certain threshold), at least one of the points must be affected by clouds. This criterion is commonly used for cloud-screening, but here it has been observed that in the presence of high aerosol loads it does not identify correctly some cloud-contaminated measurements, specially for the shorter wave-lengths. This is related to the increase in scattered radiance by aerosols for higher aerosol loads, which also leads to a lower proportion of light scattered by the clouds. Consequently, the differences between the sky radiances from two symmetric points become smaller under these sce-narios. This should be carefully considered, since this type of cloud-screening criterion, like the one used by AERONET, is usually applied to the observations used as

input in retrieval algorithms, which assume that they are not contaminated by clouds.

It has also been analysed the use of sky radiances enhanced by the presence of clouds as input for an inversion algorithm like GRASP (Generalized Retrieval of Atmosphere and Surface Properties), whose RTM assumes a cloud-free sky. For that, the inversion strat-egy'$GRASP_{pac}$' has been applied, using as input synthetic measurements under partially cloudy scenarios and their equivalent cloud-free sce-narios. In general, the optical properties are less accurate when the retrieval is conducted under the presence of clouds. This bias depends on the partially cloudy scenario, and becomes more evident when the enhancement of sky radiances due to the presence of clouds increases.

For the partially cloudy scenarios which show a significant enhancement of the sky radiances, it has been observed an underesti-mation of the aerosol absorption, introducing a bias in the single scattering albedo (SSA) of 0.05–0.06 for a low aerosol load, and of about 0.03 for extreme AOD values (equal to 1.0 at 440 nm). A lower ab-sorption seems to compensate for the excess of radiation in the sky due to clouds. The presence of clouds also induces a positive bias in the real refractive index (RRI) of 0.05–0.06 and a negative bias in the asymmetry factor (g) of about −0.02. On the other hand, a negligible effect has been observed on the aerosol size distribution parameters, and in particular for the fine mode. This is probably because the volume size distribution is mainly derived from the AOD, which in this study was assumed to be unaffected by the presence of clouds.

From all the exposed here, it is clear that the presence of clouds in the sky can significantly affect the accuracy of the aerosol properties when they are retrieved using sky radiances, even when these clouds are not in the direction of the sky points used. It is therefore recommended to be cautious with the products retrieved in these conditions. Nevertheless, these results have been obtained using synthetic data for clouds and aerosol, therefore a future scope of this work will be to conduct a similar study but with a larger number of cloudy conditions and real observations.

Funding

This work was supported by the Ministerio de Ciencia e Innovacion (MICINN), with the grant no. PID2021-127588OB-I00. This work is part of the project TED2021-131211B-I00375 funded by MCIN/AEI/10.130 39/501100011033 and European Union, "NextGenerationEU"/PRTR and is based on work from COST Action CA21119 HARMONIA. The authors acknowledge the support of the Spanish Ministry for Science and Innovation to ACTRIS ERIC. We also acknowledge the fundings from Fondo Social Europeo Plus, Programa Operativo de Castilla y Leo´n, and from the Junta de Castilla y Leon, through the Consejería de Educación.

CRediT authorship contribution statement

Sara Herrero-Anta: Writing – original draft, Validation, Methodol-ogy, Investigation, Formal analysis, Data curation, Conceptualization. **Roberto Roman:** Writing – original draft, Validation, Methodology, Investigation, Conceptualization. **Daniel Gonzalez-Fernandez:** Writing – review & editing, Methodology, Formal analysis, Data curation. **Claudia Emde:** Writing – review & editing, Software, Methodology, Data curation. **David Mateos:** Supervision, Project administration. **Celia Herrero del Barrio:** Writing – review & editing. **Ramiro Gonzalez:** Supervision. **Oleg Dubovik:** Software. **Carlos Toledano:** Supervision, Project administration, Funding acquisition. **Abel Calle:** Funding acquisition. **Victoria E. Cachorro:** Writing – review & editing, Supervision, Funding acquisition. **Bernhard Mayer:** Software. **Ángel M. de Frutos:** Funding acquisition.

Declaration of competing interest

The authors declare that they have no known competing financial interests or personal relationships that could have appeared to influence the work reported in this paper.

The author is an Editorial Board Member/Editor-in-Chief/Associate Editor/Guest Editor for *[ATMOS]* and was not involved in the edito-rial review or the decision to publish this article.

Appendix A. Supplementary data

Supplementary data to this article can be found online at https://doi. org/10.1016/j.atmosres.2025.107938.

Data availability

Data will be made available on request.

References

Barreto, A., Cuevas, E., Granados-Mun˜oz, M.J., Alados-Arboledas, L., Romero, P.M., Gro¨bner, J., Kouremeti, N., Almansa, A.F., Stone, T., Toledano, C., Roma´n, R., Sorokin, M., Holben, B., Canini, M., Yela, M., 2016. The new sun-sky-lunar cimel ce318-t multiband photometer – a comprehensive performance evaluation. Atmos. Meas. Tech. 9, 631–654. https://doi.org/10.5194/amt-9-631-2016.

Bazo, E., Granados-Mun˜oz, M.J., Roma´n, R., Bravo-Aranda, J.A., Cazorla, A., Valenzuela, A., Gonz´alez, R., Olmo, F.J., Alados-Arboledas, L., 2023. Evaluation of the vertically-resolved aerosol radiative effect on shortwave and longwave ranges using sun-sky photometer and ceilometer measurements. Atmos. Res. 282, 106517. URL. https://www.sciencedirect. com/science/article/pii/S0169809522005038. https://doi.org/10.1016/j. atmosres.2022.106517.

Boucher, O., Randall, D., Artaxo, P., Bretherton, C., Feingold, G., Forster, P., Kerminen, V.M., Kondo, Y., Liao, H., Lohmann, U., et al., 2013. Clouds and aerosols. In: Climate Change 2013: The Physical Science Basis. Contribution of Working Group I to the Fifth Assessment Report of the Intergovernmental Panel on Climate Change. Cambridge University Press, pp. 571–657.

Buras, R., Dowling, T., Emde, C., 2011. New secondary-scattering correction in disort with increased efficiency for forward scattering. J. Quant. Spectrosc. Radiat. Transf. 112, 2028–2034. URL. https://www.sciencedirect. com/science/article/pii/S0022407311001385. https://doi.org/10.1016/j. jqsrt.2011.03.019.

Dubovik, O., King, M., 2000. A flexible inversion algorithm for retrieval of aerosol optical properties from sun and sky radiance measurements. J. Geophys. Res. 105, 20673–20696.

Dubovik, O., Holben, B., Eck, T., Smirnov, A., Kaufman, Y., King, M.D., Tanre, D., Slutsker, I., 2002. Variability of absorption and optical properties of key aerosol types observed in

worldwide locations. J. Atmos. Sci. 59, 590–608.
Dubovik, O., Sinyuk, A., Lapyonok, T., Holben, B.N., Mishchenko, M., Yang, P., Eck, T.F., Volten, H., Mun˜oz, O., Veihelmann, B., van der Zande, W.J., Le´on, J.F., Sorokin, M., Slutsker, I., 2006. Application of spheroid models to account for aerosol particle nonsphericity in remote sensing of desert dust. J. Geophys. Res. 111, D11208. https://doi.org/10.1029/2005JD006619.
Dubovik, O., Lapyonok, T., Litvinov, P., Herman, M., Fuertes, D., Ducos, F., Lopatin, A., Chaikovsky, A., Torres, B., Derimian, Y., Huang, X., Aspetsberger, M., Federspiel, C., 2014. Grasp: A Versatile Algorithm for Characterizing the Atmosphere. SPIE: Newsroom. https://doi.org/10.1117/2.1201408.005558.
Dubovik, O., Fuertes, D., Litvinov, P., Lopatin, A., Lapyonok, T., Doubovik, I., Xu, F., Ducos, F., Chen, C., Torres, B., Derimian, Y., Li, L., Herreras-Giralda, M., Herrera, M., Karol, Y., Matar, C., Schuster, G.L., Espinosa, R., Puthukkudy, A., Li, Z., Fischer, J., Preusker, R., Cuesta, J., Kreuter, A., Cede, A., Aspetsberger, M., Marth, D., Bindreiter, L., Hangler, A., Lanzinger, V., Holter, C., Federspiel, C., 2021. A comprehensive description of multi-term lsm for applying multiple a priori constraints in problems of atmospheric remote sensing: Grasp algorithm, concept, and applications. Front. Remote Sens. 2 (2021). https://doi.org/10.17169/ refubium-36696.
Emde, C., Buras, R., Mayer, B., Blumthaler, M., 2010. The impact of aerosols on polarized sky radiance: model development, validation, and applications. Atmos. Chem. Phys. 10, 383–396. URL. https://acp.copernicus. org/articles/10/383/2010/. https://doi.org/10.5194/acp-10-383-2010.
Emde, C., Buras-Schnell, R., Kylling, A., Mayer, B., Gasteiger, J., Hamann, U., Kylling, J., Richter, B., Pause, C., Dowling, T., Bugliaro, L., 2016. The libradtran software package for radiative transfer calculations (version 2.0.1). Geosci. Model Dev. 9, 1647–1672. URL. https://gmd.copernicus. org/articles/9/1647/2016/. https://doi.org/10.5194/gmd-9-1647-2016.
Forster, P., Storelvmo, T., Armour, K., Collins, W., Dufresne, J., Frame, D., Lunt, D., Mauritsen, T., Palmer, M., Watanabe, M., Wild, M., Zhang, H., 2021. The Earth's energy budget, climate feedbacks and climate sensitivity. In: Masson-Delmotte, V., Zhai, P., Pirani, A., Connors, S.L., P´ean, C., Berger, S., Caud, N., Chen, Y., Goldfarb, L., Gomis, M.I., Huang, M., Leitzell, K., Lonnoy, E., Matthews, J.B.R., Maycock, T.K., Waterfield, T., Yelekçi, O., Yu, R., Zhou, B. (Eds.), Climate Change 2021: The Physical Science Basis. Contribution of Working Group I to the Sixth Assessment Report of the Intergovernmental Panel on Climate Change. Cambridge University Press, pp. 923–1054. https://doi.org/10.1017/9781009157896.009 chapter 7.
Giles, D.M., Sinyuk, A., Sorokin, M.G., Schafer, J.S., Smirnov, A., Slutsker, I., Eck, T.F., Holben, B.N., Lewis, J.R., Campbell, J.R., Welton, E.J., Korkin, S.V., Lyapustin, A.I., 2019. Advancements in the aerosol robotic network (aeronet) version 3 database – automated near-real-time quality control algorithm with improved cloud screening for sun photometer aerosol optical depth (aod) measurements. Atmospheric. Meas. Tech. 12, 169–209. URL. https://www.atmos-meas-tech. net/12/169/2019/. https://doi.org/10.5194/amt-12-169-2019.
Gonza´lez, R., Toledano, C., Roma´n, R., Fuertes, D., Berjo´n, A., Mateos, D., Guirado-Fuentes, C., Velasco-Merino, C., Antun˜a-Sa´nchez, J.C., Calle, A., Cachorro, V.E., de Frutos, A.M., 2020. Daytime and nighttime aerosol optical depth implementation in cælis. Geosci. Instrument. Methods Data Syst. 9, 417–433. URL. https://gi. copernicus.org/articles/9/417/2020/. https://doi.org/10.5194/gi-9-417-2020.
Grob, H., Emde, C., Mayer, B., 2019. Retrieval of aerosol properties from ground-based polarimetric sky-radiance measurements under cloudy conditions. J. Quant. Spectrosc. Radiat. Transf. 228, 57–72. URL. https://www.sciencedirect. com/science/article/pii/S0022407318308781. https://doi.org/10.1016/j.jqsrt.2019.02.025.
Herreras, M., Rom´an, R., Cazorla, A., Toledano, C., Lyamani, H., Torres, B., Cachorro, V., Olmo, F., Alados-Arboledas, L., de Frutos, A., 2019. Evaluation of retrieved aerosol extinction profiles using as reference the aerosol optical depth differences between various heights. Atmos. Res. 230, 104625. URL. https://www.sciencedirect.com/science/article/pii/S0169809519300432. https://doi.org/10.1016/j. atmosres.2019.104625.
Herreras-Giralda, M., Litvinov, P., Dubovik, O., Derimian, Y., Lapyonok, T., Fuertes, D., Sourdeval, O., Preusker, R., Fischer, J., 2022. Thermal emission in the successive orders of scattering (sos) radiative transfer approach. J. Quant. Spectrosc. Radiat. Transf. 291, 108327.
Herrero del Barrio, C., Roma´n, R., Gonz´alez, R., Cazorla, A., Herreras-Giralda, M., Antun˜a S´anchez, J.C., Molero, F., Navas-Guzm´an, F., Serrano, A., Obrego´n, M., Sola, Y., Pandolfi, M., Herrero-Anta, S., Gonz´alez-Ferna´ndez, D., Mun˜iz-Rosado, J., Mateos, D., Calle, A., Toledano, C., Cachorro, V.E., de Frutos, A.M., 2025. Caecenet: An automatic system processing photometer and ceilometer data from different networks to provide columnar and vertically-resolved aerosol properties. PLoS One 19 (12), e0311990. https://doi.org/10.1371/journal.pone.0311990.
Herrero-Anta, S., Rom´an, R., Mateos, D., Gonz´alez, R., Antun˜a S´anchez, J.C., Herreras-Giralda, M., Almansa, A.F., Gonz´alez-Fern´andez, D., Herrero del Barrio, C., Toledano, C., Cachorro, V.E., de Frutos, A.M., 2023. Retrieval of aerosol properties from zenith sky radiance measurements. Atmospheric. Meas. Tech. 16, 4423–4443. URL. https://amt.copernicus.org/articles/16/4423/2023/. https://doi.org/10.5194/amt-16-4423-2023.
Holben, B.N., Eck, T.F., Slutsker, I., Tanr´e, D., Buis, J.P., Setzer, A., Vermote, E., Reagan, J.A., Kaufman, Y.J., Nakajima, T., Lavenu, F., Jankowiak, I., Smirnov, A., 1998. AERONET – a federated instrument network and data archive for aerosol characterization. Remote Sens. Environ. 66, 1–16.
Holben, B.N., Eck, T.F., Slutsker, I., Smirnov, A., Sinyuk, A., Schafer, J., Giles, D., Dubovik, O., 2006. Aeronet's version 2.0 quality assurance criteria. Proc. SPIE 6408. https://doi.org/10.1117/12.706524, 64080Q8 – 14.
Jakub, F., Gregor, P., 2022. Ucla-les Shallow Cumulus Dataset with 3d Cloud Output Data. LMU Munich, Faculty of Physics. 10.57970/5d0k9-q2n86.
Lenoble, J., Herman, M., Deuz´e, J., Lafrance, B., Santer, R., Tanr´e, D., 2007. A successive order of scattering code for solving the vector equation of transfer in the earth's atmosphere with aerosols. J. Quant. Spectrosc. Radiat. Transf. 107, 479–507.
Lopatin, A., Dubovik, O., Chaikovsky, A., Goloub, P., Lapyonok, T., Tanre´, D., Litvinov, P., 2013. Enhancement of aerosol characterization using synergy of lidar and sun-photometer coincident observations: the garrlic algorithm. Atmosph. Measurem. Techniq. 6, 2065–2088. URL. https://amt.copernicus. org/articles/6/2065/2013/. https://doi.org/10.5194/amt-6-2065-2013.
Mayer, B., 2009. Radiative transfer in the cloudy atmosphere. In: EPJ Web of Conferences, EDP Sciences, pp. 75–99.
Mayer, B., Kylling, A., 2005. Technical note: the libradtran software package for radiative transfer calculations - description and examples of use. Atmos. Chem. Phys. 5, 1855–1877. URL. https://acp.copernicus. org/articles/5/1855/2005/. https://doi.org/10.5194/acp-5-1855-2005.
Roma´n, R., Benavent-Oltra, J.A., Casquero-Vera, J.A., Lopatin, A., Cazorla, A., Lyamani, H., Denjean, C., Fuertes, D., Pe´rez-Ramírez, D., Torres, B., et al., 2018. Retrieval of aerosol profiles combining sunphotometer and ceilometer measurements in grasp code. Atmos. Res. 204, 161–177.
Roma´n, R., Gonza´lez, R., Toledano, C., Barreto, A., P´erez-Ramírez, D., Benavent-Oltra, J. A., Olmo, F.J., Cachorro, V.E., Alados-Arboledas, L., de Frutos, A.M., 2020. Correction of a lunar-irradiance model for aerosol optical depth retrieval and comparison with a star photometer. Atmospheric. Meas. Tech. 13, 6293–6310. URL. https://amt.copernicus.org/articles/13/6293/2020/. https://doi. org/10.5194/amt-13-6293-2020.
Roma´n, R., Gonz´alez-Fern´andez, D., Toledano, C., Emde, C., Cachorro, V., Mateos, D., Herrero-Anta, S., Antun˜a-Sa´nchez, J., Gonza´lez, R., Antun˜a-Marrero, J., Mayer, B., Calle, A., de Frutos, A´., 2022a. Impact of clouds on cloud-free sky radiances in a partially cloudy scenario. In: International Radiation Symposium, Thessaloniki, Greece.
Roma´n, R., Antun˜a Sa´nchez, J.C., Cachorro, V.E., Toledano, C., Torres, B., Mateos, D., Fuertes, D., Lo´pez, C., Gonz´alez, R., Lapionok, T., Herreras-Giralda, M., Dubovik, O., de Frutos, A.M., 2022b. Retrieval of aerosol properties using relative radiance measurements from an all-sky camera. Atmospheric. Meas. Tech. 15, 407–433. URL. https://amt.copernicus.org/articles/15/407/2022/. https://doi. org/10.5194/amt-15-407-2022.
Salgueiro, V., Guerrero-Rascado, J., Costa, M., Roman, R., Cazorla, A., Serrano, A., Molero, F., Sicard, M., Cordoba-Jabonero, C., Bortoli, D., Comero´n, A., Couto, F., Lopez-Cayuela, M., P´erez-Ramírez, D., Potes, M., Mun˜iz-Rosado, J., Obrego´n, M., Barrag´an, R., Oliveira, D., Abril-Gago, J., Gonz´alez, R., Gíl-Díaz, C., Foyo-Moreno, I., Mun˜oz-Porcar, C., Granados-Mun˜oz, M., Rodríguez-Go´mez, A., Herreras-Giralda, M., Bravo-Aranda, J., Carvajal-Pe´rez, C., Barreto, A., Alados-Arboledas, L., 2023. Characterization of tajogaite volcanic plumes detected over the iberian peninsula from a set of satellite and ground-based remote sensing instrumentation. Remote Sens. Environ. 295, 113684. URL. https://www.sciencedirect. com/science/article/pii/S0034425723002353. https://doi.org/10.1016/j. rse.2023.113684.
Sinyuk, A., Holben, B.N., Eck, T.F., Giles, D.M., Slutsker, I., Korkin, S., Schafer, J.S., Smirnov, A., Sorokin, M., Lyapustin, A., 2020. The aeronet version 3 aerosol retrieval algorithm, associated uncertainties and comparisons to version 2. Atmospheric. Meas. Tech. 13, 3375–3411. URL. https://amt.copernicus. org/articles/13/3375/2020/. https://doi.org/10.5194/amt-13-3375-2020.
Titos, G., Ealo, M., Roma´n, R., Cazorla, A., Sola, Y., Dubovik, O., Alastuey, A., Pandolfi, M., 2019. Retrieval of aerosol properties from ceilometer and photometer measurements: long-term evaluation with in situ data and statistical analysis at montsec (southern pyrenees). Atmospheric. Meas. Tech. 12, 3255–3267. URL. https://amt.copernicus.org/articles/12/3255/2019/. https://doi. org/10.5194/amt-12-3255-2019.
Torres, B., Dubovik, O., Fuertes, D., Schuster, G., Cachorro, V.E., Lapyonok, T., Goloub, P., Blarel, L., Barreto, A., Mallet, M., Toledano, C., Tanr´e, D., 2017. Advanced characterisation of aerosol size properties from measurements of spectral optical depth using the grasp algorithm. Atmospheric. Meas. Tech. 10, 3743–3781. URL. https://www.atmos-meas-tech.net/10/3743/2017/. https://doi. org/10.5194/amt-10-3743-2017.